

THESIS APPROVED BY

Date

[Edward Goldobin], Ph.D.

Josephson Ratchet Based on YBCO Josephson Junction

EBERHARD KARLS
UNIVERSITÄT
TÜBINGEN



Physikalisches Institut

by

Alireza Jozani

Supervised by Prof. Dr. **Edward Goldobin**

July, 2023



Acknowledgments

Thank you, Thank you, Thank you, thank you, Thank you, Thank you.

To my beloved parents

Contents

Introduction	1
1 Josephson effect	3
1.1 Josephson Junction	3
1.2 Current Voltage Characteristic (IVC)	7
1.3 Josephson Junction in a Magnetic Field	9
2 Theory of Ratchet	12
2.1 An Overview of Josephson Ratchet	12
2.1.1 Josephson Ratchet Operation	14
2.1.2 Efficiency	17
2.1.3 Junctions of In-line Geometry	19
3 Fabrication and Implementation	23
3.1 Sample Information	23
3.2 Sample Layout	23
3.3 Sample Fabrication	24
3.4 He-FIB	27
3.5 Characterization	28
3.6 Implementation of an In-line Geometry Josephson Ratchet	31
4 Experimental Results	34
4.1 An Overview	34
4.2 Josephson Ratchet A22	34
4.2.1 Numerical Calculations of Ratchet A22's Parameters	42
4.3 Josephson Ratchet A15	45
4.4 Driving the Ratchet with a Stochastic Signal	50
4.4.1 External noise	50
4.4.2 Internal noise	53
4.5 Conclusion and Outlook	56

List of Tables

3.1	The maximum I_c is determined by measuring $I_c(H)$ and selecting the highest value.	29
3.2	Comparison table of target parameters between ratchet A15 and A22.	33
4.1	Comparison table of target and actual parameters of ratchet A22. Notice that we chose $\lambda = 250 \text{ nm}$ and subsequently $\lambda_{\text{eff}} = 2 \mu\text{m}$.	34
4.2	Comparison table of target and actual parameters of ratchet A15.	45
4.3	Comparison key parameters of Josephson ratchet from literature. ALJJ is the abbreviation of annular long JJ, and SQUID is the abbreviation of superconducting quantum interference device.	57

List of Figures

- | | | |
|-----|---|----|
| 1 | (a) An example of a particle trapped in a schematic asymmetric potential. (b) Schematically indicates the meaning of asymmetric. | 1 |
| 2 | The in-line geometry of a Josephson junction consists of superconducting material, where the dashed line represents the barrier JJ surrounded by superconductors. The arrows indicate the current I flowing through the superconductors. | 2 |
| 1.1 | A JJ made by the barrier potential insulator, which is formed by two closely spaced superconductors on the left and right. | 3 |
| 1.2 | Schematic electronic equivalent circuit of JJ and a RCSJ. | 5 |
| 1.3 | Plots of the tilted washboard potential $U(\varphi)$ are shown for several values of the tilt (bias current) γ . When $\gamma < 1$, the phase particle is trapped in the minimum of the potential. However, when $\gamma \geq 1$, the particle escapes from the minimum and slides down the potential. | 7 |
| 1.4 | Current-Voltage Characteristic (IVC) of a symmetric potential. | 8 |
| 1.5 | Negative and positive $I_c(\Phi_J)$ are symmetric for a fixed Φ_J . For example, when the value of Φ_J/Φ_0 is fixed at 44.5, we observe, $ I_{c+}/I_0 = I_{c-}/I_0 = 0.75$. | 11 |
| 2.1 | (a) An example of a particle trapped in a schematic asymmetric potential. (b) Schematically indicates the meaning of asymmetric. | 12 |
| 2.2 | The schematic example shows an asymmetric non-hysteretic IVC for an asymmetric Josephson potential. I_{c+} represents the positive critical current, and I_{c-} represents the negative critical current. | 13 |
| 2.3 | A rectification curve represents the average velocity of a particle ($\langle \dot{\varphi} \rangle \propto V$) as a function of the applied ac-drive amplitude I_{ac} . The interval between I_{c+} and I_{c-} is called operation interval or the rectification window, which can be defined as $\Delta \equiv I_{c-} - I_{c+}$. | 14 |
| 2.4 | A ratchet potential for $I_{dc} = 0, I_{c-}, I_{c+}$. | 15 |
| 2.5 | The schematic loaded ratchet up to countercurrent $ I_{dc} = 0.2 \mu\text{A}$. | 16 |
| 2.6 | (a) A custom-made asymmetric IVC with $\mathcal{A} = 4$. (b) The rectification curves for several values of I_{dc} based on the asymmetric IVC, borrowed from [1]. | 16 |
| 2.7 | (c) Average input ac power \bar{P}_{in} . (d) Average output dc power \bar{P}_{out} .
(e) Efficiency η , fig(4) of [1]. | 18 |

- 2.8 (a) The in-line geometry of a (JJ) consists of superconducting where the dashed line represents the barrier JJ surrounded by superconductors. The arrows indicate the current I flowing through the superconductors. 19
 (b) The current density j_L as a function of distance x .
- 2.9 A family of asymmetric $I_c(f)$ for different f^M obtained by solving the eq. (2.4) numerically. 21
- 2.10 (a) Asymmetry parameter \mathcal{A} vs. magnetic flux f for different values of f^M . (b) Asymmetry parameter \mathcal{A} vs. strength of in-line geometry f^M . 22
- 3.1 YBCO film on 2 inch LSAT substrate. (a) The scanning electron microscope picture of the sample surface. The critical temperature T_c and the value of the current density j_c are provided by Ceraco. (b) A schematic picture of the chip showing the deposition of its different layers. 23
- 3.2 The layout of the sample. The hatched light green areas correspond YBCO covered by Au, while the blue areas represent Au removal mask down to YBCO. The guide lines are also covered by Au. The Au layer is removed down to YBCO on the bridges, and two separate pads onto two parts for I & V . 24
- 3.3 Masks used during the patterned process: (a) Mask used during step (i) for the etching of gold. The blue zone indicates where the gold has been removed, leaving only YBCO. The yellow zones indicate where the gold still remains. (b) The mask used during step (ii) for the etching of YBCO. The areas in blue represent the regions where the YBCO still remains. The black area represents LSAT (substrate). Note that in the regions where the gold remains from the first step (e.g., over the pads), it has not been removed during the second step. 25
- 3.4 The microscope pictures of the sample after each step of the lithography process: (a) Picture of the pads after the step (i). The dark areas represent YBCO, and the yellow areas represent gold. (b) The picture of the bridges after the step (ii). The yellow area represents gold, the dark area represents LSAT, the blue area represents YBCO where the junction will be finally irradiated, and the purple lines are guide lines for our next step using He-FIB. 27
- 3.5 The poster of He-FIB.
- 3.6 (a) The red line indicates focused He ion beam on the atomic level with a width of the order of a few nm. (b) Schematic sketch of the BJJ produced by He-FIB, where the red line indicates the barrier JJ. 28
- 3.7 Experimental measured $j_c(D)$ (symbols) and fit (line). In total, eleven BJJ's measured with the dose $D \approx 450\ldots700$ ions/nm. The width of the BJJ's is $W = 2.8$ μm . 29
- 3.8 IVC and $I_c(H)$ of junction B28 with $D = 350$ ions/nm. 30
- 3.9 IVC and $I_c(H)$ of junction D19 with dose $D = 450$ ions/nm. 30
- 3.10 IVC and $I_c(H)$ of junction D22 with dose $D = 505$ ions/nm. 30

3.11 IVC and $I_c(H)$ of junction B33 with dose $D = 600$ ions/nm.	31
3.12 Sketch of the Josephson ratchet. The blue zone is YBCO, the red solid lines are the resistive walls, dash red line is the BJJ, and arrows indicate the flow of the supercurrent through the Josephson ratchet. w is the distance between two resistive walls and L is the length of BJJ.	31
4.1 IVC of the ratchet A22 at $I_{\text{coil}} = 0$ where $ I_{c+} \approx I_{c-} \approx 8.43 \mu\text{A}$.	35
4.2 Critical current versus magnetic coil current of the Josephson ratchet A22. We used a voltage criterion equal to $1 \mu\text{V}$ for this measurement.	36
4.3 The dependency of the value of the asymmetry parameter \mathcal{A} on I_{coil} . The maximum asymmetry, $\mathcal{A} \approx 7$ at the value of $I_{\text{coil}} \approx -69 \text{ mA}$.	37
4.4 The asymmetric IVC of ratchet A22 at the optimum magnetic field (coil current) $I_{\text{coil}} = -69 \text{ mA}$ exhibits $ I_{c+} \approx 1.53 \mu\text{A}$ and $ I_{c-} \approx -13.8 \mu\text{A}$, resulting in $\mathcal{A} \approx 7$.	38
4.5 The rectification curve for the ratchet A22 at $I_{\text{coil}} = -69 \text{ mA}$, where $ I_{c-} \approx 15.2 \mu\text{A}$, $ I_{c+} \approx 2.2 \mu\text{A}$ and $\text{RW } \Delta \approx 13 \mu\text{A}$.	38
4.6 The rectification curve for the ratchet A22 at $I_{\text{coil}} = -69 \text{ mA}$ for several I_{dc} from 0 (idle ratchet) up to $ I_{\text{dc}} = 5 \mu\text{A}$.	39
4.7 (a) $\bar{P}_{\text{in}}(I)$. (b) $\bar{P}_{\text{out}}(I)$. (c) Efficiency $\eta(I)$.	41
4.8 Simulations (lines) versus the experimental data (dots) of $\bar{V}_{\text{dc}}(I_{\text{ac}})$	43
4.9 Numerical obtained curves (lines) versus the experimental data (dots) of (a) $\bar{P}_{\text{in}}(I_{\text{ac}})$. (b) $\bar{P}_{\text{out}}(I_{\text{ac}})$. (c) $\eta(I_{\text{ac}})$.	44
4.10 IVC of the ratchet A15 at $I_{\text{coil}} = 0$. $ I_{c+} = I_{c-} \approx 21 \mu\text{A}$ and $R_N \approx 32 \Omega$.	46
4.11 Critical current versus magnetic coil current of the ratchet A15.	46
4.12 The value of asymmetry parameter, which shows the maximum asymmetry $\mathcal{A} \approx 7$ at optimum magnetic $I_{\text{coil}} = 75 \text{ mA}$.	47
4.13 An asymmetric IVC of the ratchet A15 at the optimum $I_{\text{coil}} = 75 \text{ mA}$ has $ I_{c-} \approx 24.5 \mu\text{A}$ and $ I_{c+} \approx 3.5 \mu\text{A}$.	47
4.14 The rectification curve $\bar{V}_{\text{dc}}(I_{\text{ac}})$ for the ratchet A15 at $I_{\text{coil}} = 75 \text{ mA}$ with maximum dc average voltage $\bar{V}_{\text{dc}}(I_{\text{ac}}) \approx 225 \text{ V}$.	48
4.15 Simulations (lines) versus the experimental data (dots) of $\bar{V}_{\text{dc}}(I_{\text{ac}})$ for the loaded ratchet A15 at $I_{\text{coil}} = 75 \text{ mA}$ for several I_{dc} up to stopping force $ I_{\text{dc}} = 8.92 \mu\text{A}$.	48
4.16 Numerical obtained curves (lines) versus the experimental data (dots) of (a) \bar{P}_{in} , (b) \bar{P}_{out} , (c) Efficiency η .	49
4.17 (a) The Gaussian distribution of random signal with the width σ . (b) The random signal depends on time.	50
4.18 Simulation of $\bar{V}_{\text{dc}}(\sigma)$ driven with the Gaussian signal.	51
4.19 (a) $\bar{P}_{\text{in}}(\sigma)$. (b) $\bar{P}_{\text{out}}(\sigma)$. (c) Efficiency η .	52
4.20 IVC of A15 at $T \approx 4.2 \text{ K}$ and 35 K at zero magnetic field $I_{\text{coil}} = 0$.	53
4.21 IVC for the ratchet A15 at around temperature 35 K for the two values of I_{coil} : zero and the optimum magnetic field. In the lower right, we zoom in on the origin.	54
4.22	55

Introduction

Typically, when referring to a ratchet system or equivalently Brownian motor, one can envision a system characterized by an interaction with a surrounding large bath where symmetric nature of the potential is broken, and a periodic asymmetric potential would be immediately used to describe the ratchet system (e.g., see the schematic Fig. 1). It has been demonstrated [2] that in the system, where a particle is trapped in an asymmetric potential, directed transport is induced by unbiased, driving forces with zero time average. This allows the particle to perform useful work under some specific conditions. The system could be driven by an additional stochastic perturbation, which, e.g., is caused by a non-negligible influence of thermal noise. These effects would be captured and studied.

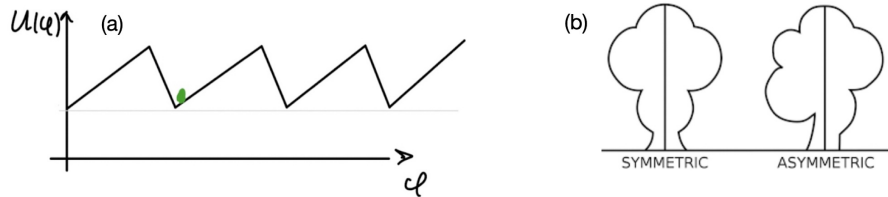


Figure 1: (a) An example of a particle trapped in a schematic asymmetric potential. (b) Schematically indicates the meaning of asymmetric.

This master's thesis focuses on the investigation of the Josephson ratchet based on High Temperature Superconductors (HTSs), namely YBCO, fabricated (designed) using a Helium focused ion Beam (He-FIB) technique. Roughly speaking, a Josephson ratchet is a device, which is based on a Josephson junction of an in-line geometry (e.g., see Fig. 2), where the particle is trapped in the asymmetric potential.

In this thesis, the Josephson ratchet was experimentally driven in both deterministic and stochastic regimes. Subsequently, we explored the effects of external and internal noises, with a particular emphasis on the dominance of time-dependent perturbations.

As an **application**, the recent surge of interest has been focused on superconductor diodes, which serve as an equivalent realization of the Josephson ratchets. For instance, reference [3] presents a notable realization of a particle trapped within a Josephson asymmetric potential. However, in this thesis, we demonstrate that Josephson ratchets generally exhibit higher efficiency and a smaller device footprint.

The thesis is organized as follows:

In Chapter. 1, the concept of the Josephson effect with a 2π periodic gauge-invariant phase in the presence of a magnetic field is carefully examined, with a specific focus on a particle trapped in a symmetric potential.

In Chapter. 2, we will first undertake a theoretical investigation of how a particle trapped in an asymmetric Josephson potential can be operated to generate useful work with a specific level of efficiency [1] [4]. Furthermore, the dependency of critical current on the magnetic field is numerically simulated for a specific geometry (an In-line geometry of Josephson junction) to gain initial insights into the required design parameters for a Josephson ratchet.

In Chapter. 3, the focus shifts to the fabrication of the sample. The lithography process and irradiation techniques, such as He-FIB, are employed in the fabrication of the Josephson ratchet. Subsequently, we present the current density characterization of our samples.

In Chapter. 4, we present the experimental results of two Josephson ratchet devices operating in different regimes: deterministic (i.e., when the system is driven with a sinusoidal drive) and stochastic (i.e., when the Josephson ratchet is driven with a randomly varying signal, such as noise). We measure such figures of merits \bar{V}_{dc} , \bar{P}_{out} , \bar{P}_{in} , and the efficiency. Furthermore, since we operate in a quasi-static regime, we can simulate all the ratchet parameters based on the experimental current-voltage characteristics. Notably, we investigate how external noise affects the particle's dynamics in an asymmetric potential, enabling ratchet operation. Lastly, we explore the influence of internal noise, modeled as a random signal following the Gaussian distribution.

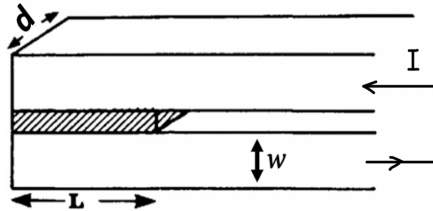


Figure 2: The in-line geometry of a Josephson junction consists of superconducting material, where the dashed line represents the barrier JJ surrounded by superconductors. The arrows indicate the current I flowing through the superconductors.

In conclusion, we summarize our work concisely and provide an **outlook** on future research directions.

Chapter 1

Josephson effect

1.1 Josephson Junction

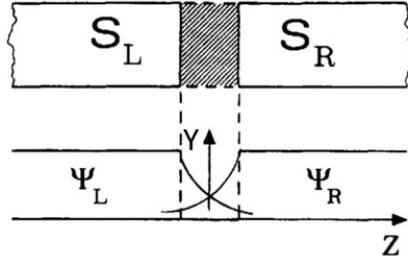


Figure 1.1: A JJ made by the barrier potential insulator, which is formed by two closely spaced superconductors on the left and right.

The Josephson effect is a phenomenon that describes the flow of supercurrent, which is a current without dissipation, between two separated superconductors. When two superconductors, denoted as S_L and S_R , are brought close together with only a small gap and a barrier separating them, a continuous supercurrent flows between them. This device is known as a Josephson junction (JJ), as shown schematically in Fig. 1.1. The left superconductor has a wave function of Cooper pairs (a pair of electrons or other fermions bound together at low temperatures) $\psi_L(t, \mathbf{x}) = |\psi_0| e^{i\phi_L(t, \mathbf{x})} = \sqrt{n_{s,L}} e^{i\phi_L(t, \mathbf{x})}$.¹ Similarly, the wave function for the right superconductor, S_R , is given by $\psi_R(t, \mathbf{x}) = |\psi_0| e^{i\phi_R(t, \mathbf{x})} = \sqrt{n_{s,R}} e^{i\phi_R(t, \mathbf{x})}$. If the potential difference across the junction is V , then the potential energy difference between the two superconductors is $2eV$, since each Cooper pair has twice the charge of an electron. The Schrödinger equation for these two quantum states, ψ_L and ψ_R , is as follows

$$i\hbar \frac{\partial}{\partial t} \begin{pmatrix} \sqrt{n_{s,L}} e^{i\phi_L} \\ \sqrt{n_{s,R}} e^{i\phi_R} \end{pmatrix} = \begin{pmatrix} eV & K \\ K & -eV \end{pmatrix} \begin{pmatrix} \sqrt{n_{s,L}} e^{i\phi_L} \\ \sqrt{n_{s,R}} e^{i\phi_R} \end{pmatrix}, \quad (1.1)$$

¹Throughout this work, the bold symbol, \mathbf{x} , represents a three-dimensional vector, and ψ is a vector field which represents our wave function.

where K is an interaction coupling constant that represents the strength of the interaction coupling between the wave functions of the two superconductors, $n_{s,i}$ ($i = L$ or R) is the charge carrier density (Cooper pair density) which is proportional to the current I through the supercurrent density $\vec{j}_s = q_s \cdot n_s \cdot \vec{v}_s$, where \vec{v}_s is the velocity vector of the Cooper pairs, q_s is the Cooper charge, and S_J is the surface area of the Josephson junction, which will be precisely defined once we define the geometry of JJ later in this chapter. After taking the derivative of eq. (1.1) and splitting the real and imaginary parts, we obtain the following set of equations for ϕ_L , ϕ_R , $n_{s,L}$, and $n_{s,R}$ [5]

$$\begin{aligned}\dot{n}_{s,L} &= \frac{2K}{\hbar} \sqrt{n_{s,L} n_{s,R}} \sin(\phi_L - \phi_R), \\ \dot{n}_{s,R} &= -\frac{2K}{\hbar} \sqrt{n_{s,L} n_{s,R}} \sin(\phi_L - \phi_R),\end{aligned}\tag{1.2}$$

$$\begin{aligned}\dot{\phi}_L &= \frac{K}{\hbar} \sqrt{\frac{n_{s,L}}{n_{s,R}}} \cos(\phi_L - \phi_R) + \frac{eV}{\hbar}, \\ \dot{\phi}_R &= \frac{K}{\hbar} \sqrt{\frac{n_{s,R}}{n_{s,L}}} \cos(\phi_L - \phi_R) - \frac{eV}{\hbar}.\end{aligned}\tag{1.3}$$

The phase differences between two superconductors is defined $\varphi_0 \equiv \phi_L - \phi_R$ (without presence of a magnetic field). Thus, the differences of $\dot{\varphi}_0 \equiv \dot{\phi}_L - \dot{\phi}_R$ yields the 2nd Josephson equation as follows

$$\frac{\partial \varphi_0(t, \mathbf{x})}{\partial t} = \frac{2eV(t)}{\hbar} = \frac{2\pi V}{\Phi_0},\tag{1.4}$$

where $\Phi_0 = \frac{h}{2e} \approx 2.068 \times 10^{-15}$ Wb is magnetic flux quantum. Eq. (1.4) describes the linear evolution of phase differences across the junction for constant applied voltage. It immediately follows from eq. (1.4) that if there is no voltage across the junction i.e., $V = 0$, then φ_0 is constant. This implies constant arguments of the angular functions in eq. (1.2), and thus $\dot{n}_{s,L} = -\dot{n}_{s,R}$. Therefore, if $n_{s,L} = n_{s,R}$, then $n_{s,i} = \text{const}$, and the current should flow uniformly (in time) between the two superconductors. Otherwise, the superconductors would be charged, and the supercurrent would flow non-uniformly. Thus, the supercurrent density depends on the phase difference $j_s(\varphi_0)$, which must be gauge invariant. That is, in the presence of the magnetic field, the supercurrent density becomes as ²

$$j_s(\psi) = q_s \operatorname{Re} \left\{ \psi^* \left(\frac{\hbar}{mi} \vec{\nabla} - \frac{q_s}{m} \vec{A} \right) \psi \right\} = \frac{q_s n_s \hbar}{m_s} \vec{\nabla} \varphi,$$

where in the last equality we have inserted the definition of Cooper pair wave function and defined φ such as $\vec{\nabla} \varphi := \vec{\nabla} \varphi_0 - \frac{2\pi}{\Phi_0} \vec{A}$, which is the gauge invariant phase

²The Schrödinger equation implies the continuity equation $\left(\frac{\partial |\psi(t, \mathbf{x})|^2}{\partial t} = -\vec{\nabla} \cdot j(t, \mathbf{x}) \right)$, where the probability current density can be defined as $j_s(\psi)$. [6]

differences in the presence of magnetic field³. Now if we integrate this gauge invariant phase differences over the area of the barrier Josephson junction, we obtain $\varphi(t, \mathbf{x}) = \varphi_0 - \frac{2\pi}{\Phi_0} \int_L^R A_y(\mathbf{x}) dx$, where A_y is a homogeneous magnetic vector potential in the y -direction. Since φ is a gauge invariant phase, the direction of the magnetic field does not matter, but it must be perpendicular to the surface of the JJ. Additionally, we note that inside the junction, $\psi(t, \mathbf{x})$ is defined modulo 2π (i.e., $\psi(t, \mathbf{x}) = \sqrt{n_s} e^{i(\varphi(t, \mathbf{x}) + 2\pi)} = \sqrt{n_s} e^{i\varphi(t, \mathbf{x})}$), so phase changes by $2n\pi$ (n is an integer) do not change the wave function ψ . Furthermore, $j_s(\varphi)$ is time reversal invariant ($j_s(\varphi) = -j_s(-\varphi)$).

Taking all these considerations into account, we define the uniform gauge invariant supercurrent density as an odd, 2π -periodic function of the phase difference, i.e., $j_s(\varphi) = j_s(\varphi + 2n\pi)$. Thus, the first Josephson equation can be defined as follows

$$I_s := I_0 \sin [\varphi(t)]. \quad (1.5)$$

This is the supercurrent, which flows uniformly between the two superconductors and is referred to as the Josephson supercurrent. In the eq. (1.5), I_0 is the maximum supercurrent that can flow through JJ and is known as the critical current. [8]

In a typical JJ experiment, we usually apply a current that flows through the JJ and then we measure the resulting output dc voltage. A commonly used electrical circuit model for measuring the voltage across the Josephson junction is called the Resistively and Capacitively Shunted Junction (RCSJ) model. This model assumes an equivalent circuit schematically depicted in Fig. 1.2.

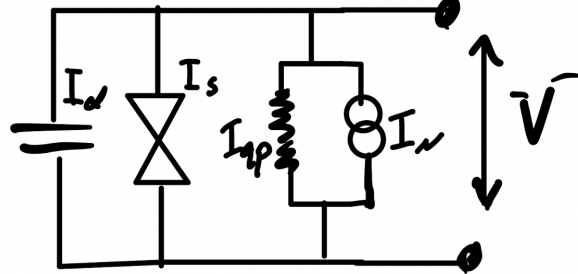


Figure 1.2: Schematic electronic equivalent circuit of JJ and a RCSJ.

According to Kirchhoff's law one can write the constant total current $I = I_d + I_{qp} + I_s + I_n$ ⁴, which is coming from the current source divides into four components, (I) The supercurrent $I_s = I_0 \sin [\varphi(t)]$;

³Here by gauge invariant phase we mean, e.g., that the expression $\vec{\nabla}\varphi(t, \mathbf{x})$ will remain unchanged under using gauge transformations, that is, if we transform $\varphi_0(t, \mathbf{x}) \rightarrow \varphi_0(t, \mathbf{x}) + \frac{q_s}{\hbar}\chi(\mathbf{x})$ and $\vec{A}(t, \mathbf{x}) \rightarrow \vec{A}(t, \mathbf{x}) + \vec{\nabla}\chi(\mathbf{x})$, where $\chi(\mathbf{x})$ is any scalar field, we would see that the phase and subsequently supercurrent density will be invariant under these transformations. For more detail see the Ginzburg–Landau theory. [7]

⁴This constant current arises from the conservation law of net charge in the components.

- (II)** Dissipative (quasiparticle) current at normal electrodes $I_{qp} = \frac{V}{R_N}$; where R_N is a resistor at the barrier;
- (III)** Displacement current $I_D = C_J \dot{V}$; where C_J is a capacitance across junction;
- (IV)** At finite temperature T , the resistance simultaneously generates a thermal noise, which is represented by Johnson–Nyquist noise current source I_n parallel to the R in Fig. 1.2. It refers to the random fluctuations with Gaussian distribution that arise due to the thermal energy and agitation of electrons in the resistances. Here the current source in shunt is given by $i_n = \sqrt{\frac{4k_B T \Delta f}{R}}$, where Δf is the bandwidth in hertz over which the noise is measured. We will investigate it experimentally later on in Chapter 4.

By neglecting the thermal noise sources in Fig. 1.2

$$I = I_0 \sin [\varphi(t)] + \frac{V(t)}{R_N} + C_J \frac{dV(t)}{dt}, \quad (1.6)$$

which can be rewritten using eq. (1.4) via Josephson phase, φ instead of V as

$$I = I_0 \sin (\varphi) + \frac{1}{R_N} \frac{\Phi_0}{2\pi} \dot{\varphi} + C_J \frac{\Phi_0}{2\pi} \ddot{\varphi}. \quad (1.7)$$

One can also derive the eq. (1.7) as the equation of motion (EoM) of a particle with coordinate φ moving in a potential energy $U(\varphi)$, using the Euler–Lagrange equation. The Josephson potential energy $U(\varphi)$ can be written as a cosinusoidal function

$$U(\varphi) \equiv E_J(1 - \cos \varphi - \gamma \varphi), \quad (1.8)$$

where $\gamma \equiv I/I_0$ represents the normalized bias current, and $E_J \equiv I_0 \Phi_0 / 2\pi$ is the so-called Josephson coupling energy. Fig. 1.3 illustrates the Josephson potential for different values of the γ . We observe that when $\gamma = 0$, the potential is mirror-symmetric (purple curve), and as γ increases, the potential becomes tilted. The shape of $U(\varphi)$ resembles an old-fashioned washboard, thus it is referred to as a tilted washboard potential. It is evident that the tilt of the potential arises from γ . Specifically, the particle’s phase motion on the purple, green, and red curves, where $0 \leq \gamma < 1$ exhibits periodic oscillation. On the blue curve with $\gamma \geq 1$, however, the particle does not exhibit periodic oscillation [9].

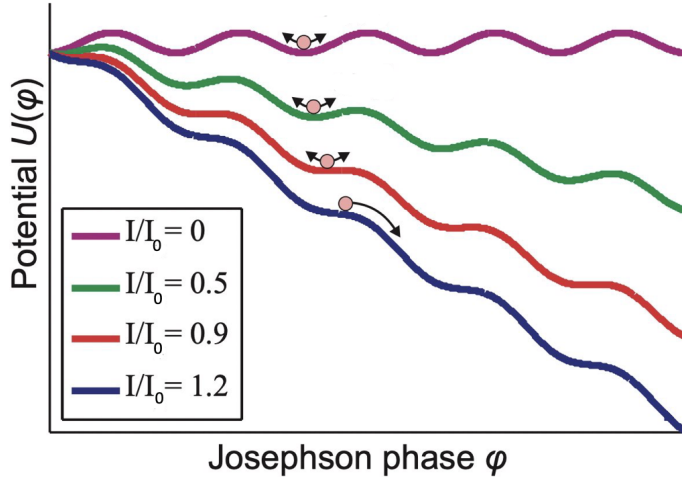


Figure 1.3: Plots of the tilted washboard potential $U(\varphi)$ are shown for several values of the tilt (bias current) γ . When $\gamma < 1$, the phase particle is trapped in the minimum of the potential. However, when $\gamma \geq 1$, the particle escapes from the minimum and slides down the potential.

It is often practical to use normalized units, therefore we introduce a new normalized time $\tau \equiv \frac{t}{\tau_c} = \frac{t}{2\pi e I_0 R} \Phi_0$. So that eq. (1.7) becomes

$$-\gamma + \sin [\varphi(\tau)] + \frac{d\varphi}{d\tau} + \beta_c \frac{d^2\varphi}{d\tau^2} = 0, \quad (1.9)$$

where $\beta_c \equiv \frac{\omega_c^2}{\omega_p^2} = \frac{2\pi}{\Phi_0} I_0 R_N^2 C$ is so called Stewart-McCumber parameter.

1.2 Current Voltage Characteristic (IVC)

Now let us see how a dc current-voltage characteristic (IVC) of the JJ looks like. In an experiment, we typically apply different values of dc currents I and measure an average (dc) voltage across the junctions for each current value of I , denoted as $\bar{V}(I)$. Using the known periodic phase evolution $\varphi(t)$, which can be obtained by solving the eq. (1.9) for $\varphi(t)$, the average voltage can be calculated as follows

$$\bar{V}(I) = \frac{1}{T} \int_0^T V(t) dt \stackrel{(1.4)}{=} \frac{1}{T} \int_0^T \frac{\Phi_0}{2\pi} \frac{d\varphi}{dt} dt = \frac{1}{T} \frac{\Phi_0}{2\pi} \overbrace{[\varphi(T) - \varphi(0)]}^{2\pi} = \frac{\Phi_0}{T}, \quad (1.10)$$

where we use 2nd Josephson equation in the second equality. The parameter $T = \frac{2\pi}{\omega}$ represents the time it takes for a particle to complete one period of the potential shown in Fig. 1.3. Eq. (1.9) and (1.10) together can be used to obtain the typical IVC for different values of β_c as shown in Fig. 1.4

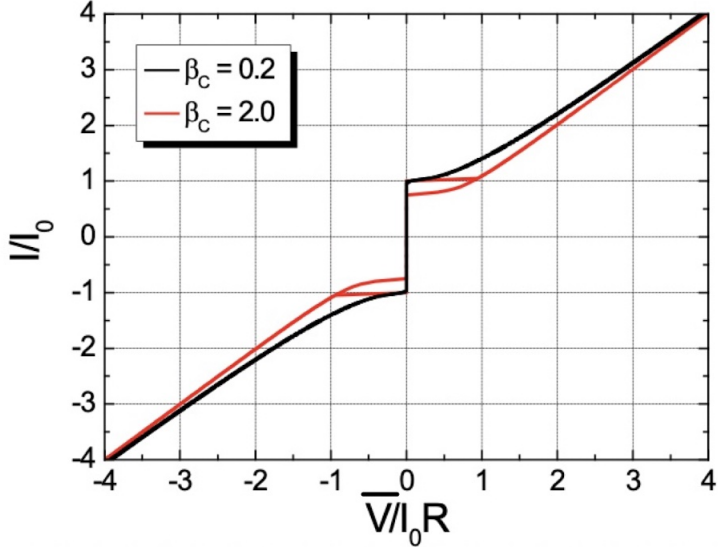


Figure 1.4: Current-Voltage Characteristic (IVC) of a symmetric potential.

For $\beta_c \ll 1$, where friction term $\dot{\varphi}$ dominates, one can neglect the last term ($\beta_c \ddot{\varphi}$) in the eq. (1.9). This leads to a non-hysteretic IVC, represented by the black curve in Fig. 1.4. In this case, one can determine the time it takes for the particle to complete one period of the tilted potential as $T = \frac{2\pi\tau_c}{\sqrt{\gamma^2 - 1}}$ and calculate the averaged voltage,

$$\bar{V} = \begin{cases} I_0 R \sqrt{\gamma^2 - 1} & \text{if } \gamma > 1, \\ -I_0 R \sqrt{\gamma^2 - 1} & \text{if } \gamma < -1, \\ 0 & \text{otherwise.} \end{cases} \quad (1.11)$$

For $\beta_c \gg 1$, the inertia term $\ddot{\varphi}$ in eq. (1.9) becomes dominant, resulting in a hysteretic IVC (the red curve in Fig. 1.4). In this case, one can investigate how the thermal fluctuation noise can characterize and adjust the hysteresis observed in the red curve shown in Fig. 1.4. This can be achieved by incorporating $I_n(t)/I_0$ into the γ term in the potential eq. (1.8). The characterization of this effect can be quantified through a thermal noise parameter defined as [9]

$$\Gamma \equiv \frac{K_B T}{E_J} = \frac{2\pi K_B T}{I_0 \Phi_0} = \frac{I_{\text{th}}}{I_0}. \quad (1.12)$$

To this end, we would like to highlight that the IVC is completely symmetric. In other words, $\bar{V}(I) = -\bar{V}(-I)$. [9]

1.3 Josephson Junction in a Magnetic Field

In the following, we will study the dependence of the IVC on the externally applied magnetic field, denoted as H , to the JJ. Specifically, we are interested in the dependence of $I(H)$. Firstly, we will determine how magnetic field affects the gauge invariant phase differences across the barrier JJ. Then, we will incorporate the phase differences across the JJ $\varphi(t, \mathbf{x})$ into the definition of the supercurrent density $j_s(\varphi)$. Finally, we will integrate it over the area of JJ to obtain the total supercurrent over the junction, denoted as $I_s(H) = \int_{S_J} j_s(\varphi) d\mathbf{x}$. This $I_s(H)$ may take a range of values. Our objective is to determine the minimum or maximum value corresponding to I_c . In [9], the author considers a JJ with a rectangular geometry for simplicity and demonstrates how the applied magnetic field induces a gradient of phase differences φ , as given by

$$\frac{d\varphi}{dx} = \frac{2\pi}{\Phi_0} Bd_{\text{eff}}, \quad (1.13)$$

where $d_{\text{eff}} = d + 2\lambda \tanh(d/\lambda)$ is the effective magnetic thickness of the JJ, d is the thickness of BJJ, and λ is the London penetration depth. Without loss of generality, we assume a homogeneous and uniform applied magnetic field, denoted as $B(t, \mathbf{x}) \equiv B(x)$, which is applied along y -direction, $B(x) \equiv B_y(x)\hat{y}$, and is perpendicular to the JJ plane, defined by the (x, z) coordinates. Additionally, we observe that by the Ampère–Maxwell equation, we have $\vec{\nabla} \times B_y = \frac{\partial B_y(x)}{\partial x}\hat{z} = \mu_0 j_z(x)$. By taking derivative of eq. (1.13) with respect to x and using the Ampère–Maxwell equation, we obtain

$$\frac{\partial^2 \varphi(\mathbf{x})}{\partial x^2} = \frac{2\pi}{\Phi_0} d_{\text{eff}} \frac{\partial B_y(\mathbf{x})}{\partial x} = \frac{1}{\lambda_J^2} \frac{j_z(\mathbf{x})}{j_0} = \frac{1}{\lambda_J^2} \sin \varphi(\mathbf{x}), \quad (1.14)$$

where λ_J is so called the Josephson penetration depth⁵, which is defined as follows

$$\lambda_J \equiv \left(\frac{\Phi_0}{2\pi\mu_0 d_{\text{eff}} j_0} \right)^{1/2}. \quad (1.15)$$

We notice that for small applied magnetic field we can use Taylor expansion ($\sin \varphi \approx \varphi$) and solve eq. (1.14) to obtain $\varphi(x) = \varphi(0)e^{-x/\lambda_J}$. Now if we assume that our junction has length L smaller than Josephson penetration depth λ_J , then B_y fully penetrates into the JJ and becomes constant i.e., $B(x) \approx \text{const}$. Therefore, we consider a uniform magnetic field, which homogeneously penetrates into the JJ and allows us to take the integral of eq. (1.13) by pulling B out of the integral and obtain

$$\varphi(t, \mathbf{x}) = \varphi_0 + \frac{2\pi}{\Phi_0} Bd_{\text{eff}}x. \quad (1.16)$$

⁵Notice that this calculation of λ_J is only valid for thick electrode e.g., $x > \lambda$. In the λ_J stays inductance which is equal to $\mu_0 d_{\text{eff}}$ only if $d_{\text{eff}} = 2\lambda$.

Hence one can rewrite the eq. (1.5) as follows

$$I(\mathbf{x}) = \int_{S_J} j_c(\mathbf{x}) \sin(\varphi(t, \mathbf{x})) d\mathbf{x}, \quad (1.17)$$

where $j_c(\mathbf{x})$ is a critical current density, which can be uniformly (e.g., $j_c(\mathbf{x}) = \text{const}$) or non-uniformly (e.g., $j_c(x, y)$) distributed. Therefore, the critical current density can be achieved by selecting a specific geometry and considering the presence of a magnetic field. The behavior of the supercurrent is investigated in [8] for various choices of current density and geometry. One can rewrite eq. (1.17) for a rectangular geometry of a BJJ (e.g., for a JJ with length $|x| \leq L/2$ and width W) as

$$I(x) = W \int_{-L/2}^{L/2} j_c(x) \sin(\varphi) dx = W \operatorname{Im} \left\{ e^{i\varphi_0} \int_{-L/2}^{L/2} j_c(x) e^{i2\pi Bd_{\text{eff}}x/\Phi_0} dx \right\}. \quad (1.18)$$

To obtain the maximum supercurrent, the eq. (1.18) should be maximized with respect to φ_0 , $\left| \frac{dI}{d\varphi_0} = 0 \right|$. We obtain

$$I = W \left| \int_{-L/2}^{L/2} j_c(x) e^{i2\pi Bd_{\text{eff}}x/\Phi_0} dx \right|. \quad (1.19)$$

This is the maximum Josephson current at any given applied magnetic field, H . Now if we assume a uniform critical current distribution i.e., $j_c(x) = \text{const}$ inside the JJ, then the eq. (1.19) yields the well-known Fraunhofer dependence.

$$I_c(\Phi_J/\Phi_0) = I_0 \cdot \left| \frac{\sin\left(\pi \frac{\Phi_J}{\Phi_0}\right)}{\pi \frac{\Phi_J}{\Phi_0}} \right| = I_0 \cdot \left| \operatorname{sinc}\left(\pi \frac{\Phi_J}{\Phi_0}\right) \right|, \quad (1.20)$$

where $\Phi_J = Bd_{\text{eff}}L$ is the total magnetic flux inside the junction and $I_0 = j_c \times S_J = j_c \cdot W \cdot L$. Eq. (1.20) can be rewritten for all values of Φ_J as

$$I_c\left(\pm(\Phi_J/\Phi_0)\right) = \pm I_0 \cdot \left(\operatorname{sinc}\left(\pi \frac{\Phi_J}{\Phi_0}\right) \right),$$

which can be plotted as shown in Fig. 1.5. The signs also indicate maximum (I_{c+}) and minimum (I_{c-}) critical currents.

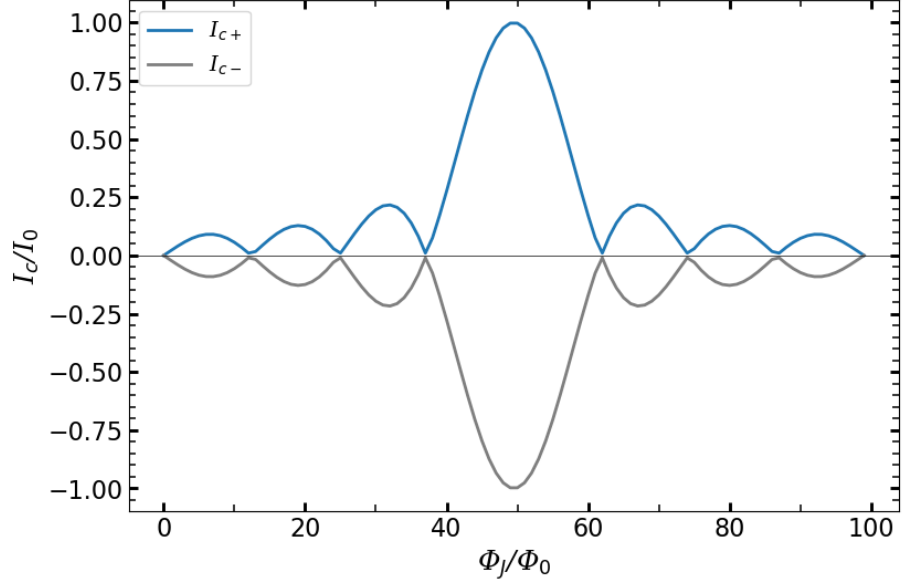


Figure 1.5: Negative and positive $I_c(\Phi_J)$ are symmetric for a fixed Φ_J . For example, when the value of Φ_J/Φ_0 is fixed at 44.5, we observe, $|I_{c+}/I_0| = |I_{c-}/I_0| = 0.75$.

Finally, we would like to point out that the $I_c\left(\pm(\Phi_J/\Phi_0)\right)$ values are symmetric with respect to the current polarity. In other words, for any fixed value of the flux Φ_J we find that $|I_{c+}| = |I_{c-}|$. [8]

Chapter 2

Theory of Ratchet

2.1 An Overview of Josephson Ratchet

When discussing a ratchet, the simplest model we have in mind is a periodic asymmetric potential¹ where a particle moves under the action of stochastic force with zero time averaged, as shown in fig. 2.1 (a). Such a force pushes the particle back and forth, but on average, the force does not push the particle anywhere forward or backward. However, due to the asymmetry of the potential, in some cases, one can observe a net transport in a particular direction. Consequently, the random force with zero time average can be transformed into directed particle motion, enabling the particle to perform useful work. We will delve further into this concept in the subsequent sections of this chapter.

Since we will consider Josephson system in this thesis, the particle will move in the potential along the coordinate φ . Therefore, the averaged velocity $\langle \dot{\varphi} \rangle$ of the particle, is proportional to the averaged voltage, as described by eqe. (1.4). Similarly, when we mention the application of current, as indicated in eq. (1.7), it is analogous to applying a force.² Hence, when we mention the application of a dc current to the system, it is synonymous with applying forces.

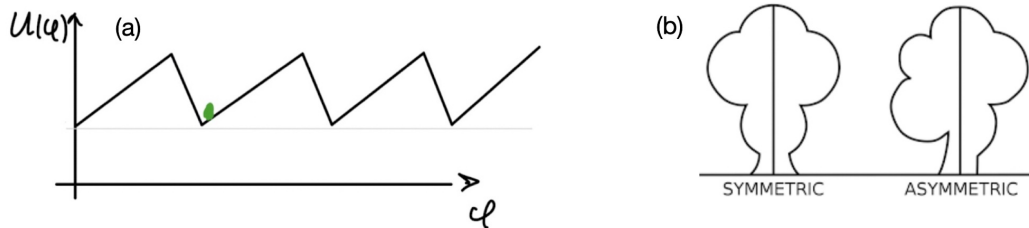


Figure 2.1: (a) An example of a particle trapped in a schematic asymmetric potential. (b) Schematically indicates the meaning of asymmetric.

¹by asymmetrical, we mean reflexion asymmetry, $U(-\varphi) \neq U(\varphi)$.

²The Newtonian force for a stationary potential can be written as $F = -\nabla_\varphi U(\varphi)$. Now if we use the Josephson potential eq. (1.8), we would get $F \propto \gamma$, which means that applied current is proportional to force.

So far, we have studied the symmetric Josephson potential in detail, as seen in eq. (1.8), and Fig. 1.3. However to construct a Josephson ratchet, we need to design an asymmetric Josephson potential. We schematically show this kind of potential in Fig. 2.1(a).

Similar to Chapter 1.1, in order to determine the IVC, one can derive the dependency of the averaged voltage on the current from an EoM analogous to eq. (1.9), but this time for an asymmetric Josephson potential instead of symmetric potential. A non-hysteretic IVC for the asymmetric potential is schematically depicted in Fig. 2.2.

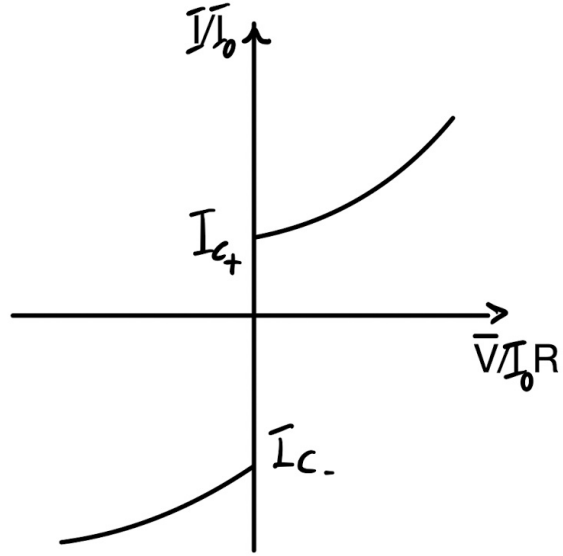


Figure 2.2: The schematic example shows an asymmetric non-hysteretic IVC for an asymmetric Josephson potential. I_{c+} represents the positive critical current, and I_{c-} represents the negative critical current.

We clearly observe that $|I_{c-}| \neq |I_{c+}|$, resulting in an asymmetric IVC, which is in contrast to what we obtained for the symmetric Josephson potential. This inequality in I_c values is attributed to the fact that in the asymmetric potential, the maximum slopes of the potential in the left/right directions are different. Therefore, the force (applied current) needed to overcome this slope (critical current) is also different for each polarity. We can now quantify the degree of asymmetry by using the symmetry parameter \mathcal{A} . This parameter is generally defined as the ratio of the maximum slopes of the potential in the left and right directions

$$\mathcal{A} \equiv \frac{\max(|I_{c+}|, |I_{c-}|)}{\min(|I_{c+}|, |I_{c-}|)}. \quad (2.1)$$

Later, we will see that \mathcal{A} is one of the key parameters defining the performance of the ratchet.

2.1.1 Josephson Ratchet Operation

If the IVC exhibits a similar characteristic as shown in Fig. 2.2, it is possible to operate a ratchet in the deterministic regime and construct a rectifier. Typically, a rectifier is achieved by applying an ac signal and obtaining a dc output signal. In our specific case, we apply an ac current and observe the ratchet effect through the response of the dc output. This effect can be accurately interpreted using a rectification curve $\langle V \rangle(I_{ac})$. Fig. 2.3 schematically illustrates this rectification curve.

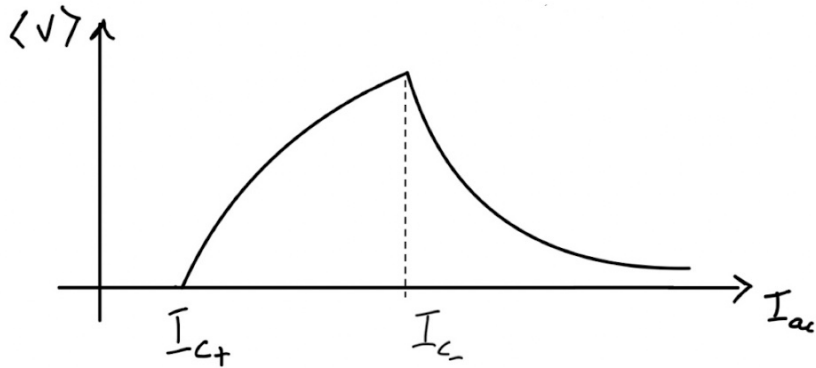


Figure 2.3: A rectification curve represents the average velocity of a particle ($\langle \dot{\phi} \rangle \propto V$) as a function of the applied ac-drive amplitude I_{ac} . The interval between I_{c_+} and I_{c_-} is called operation interval or the rectification window, which can be defined as $\Delta \equiv I_{c_-} - I_{c_+}$.

When an alternating current $I(t) = I_{ac} \sin(\omega t)$ is applied, it can be understood as tilting the potential back and forth at a frequency of ω . However, for small tilting amplitudes $I_{ac} < |I_{c_-}|$, we find that the particle remains trapped within the potential well, resulting in an average velocity (voltage) equaled to zero. For $I_{ac} > |I_{c_+}|$, the particle starts moving forward until it reaches its maximum average velocity at $I_{ac} \rightarrow |I_{c_-}|$. As I_{ac} is further increased, the average voltage gradually decreases until it eventually approaches zero. The range between I_{c_+} and I_{c_-} is known as the rectification window (RW), representing the interval during which the particle can move during a fraction of the positive and not move (remain trapped) during the negative semi-periods of the ac drive.

We observe that a larger asymmetry parameter results in a wider RW. In the absence of asymmetry (i.e., in the case of a symmetric Josephson potential with $\mathcal{A} = 1$ or $|I_{c_+}| = |I_{c_-}|$), the rectification curve (average velocity) remains zero, and the particle does not move in average. This occurs because the net average force exerted on the particle from both left and right sides of the symmetric potential well is zero. This can be seen, for example, in the purple curve depicted in Fig. 1.3.

A relevant question arises: How good is a ratchet? How can we characterize its performance? Obviously, we want a ratchet to work not only for a certain amplitudes of the input signal, but for a very wide range of amplitudes, ideally from a small

amplitude to a very large amplitude. However, as we saw in Fig. 2.3 the ratchet does not move for the small and very large amplitudes, and there is only a limited range of amplitudes (the RW), in which the rectification occurs ($\langle V \rangle \neq 0$). Therefore, to achieve a broad operational range for the ratchet, we aim to maximize the size of the RW. This entails minimizing $|I_{c+}|$ and maximizing $|I_{c-}|$. Consequently, a larger asymmetry parameter \mathcal{A} leads to an expanded interval of operation, enabling a wider range of amplitudes in which the ratchet can function effectively.

However, even if the ratchet is capable of rectification, it does not yet generate useful work or deliver rectified power to a load. We refer to such a ratchet as being idle. To prevent the ratchet from being idle, we should load it i.e., by applying counterforce, typically in the form of a dc current I_{dc} . This counterforce tilts the potential and pushes the particle in the opposite direction to the ratchet motion. If the ratchet effect is stronger than this counterforce, the particle overcomes the constant (counter) slope and ascends, thereby performing useful work. Fig. 2.4 schematically depicts a loaded ratchet.

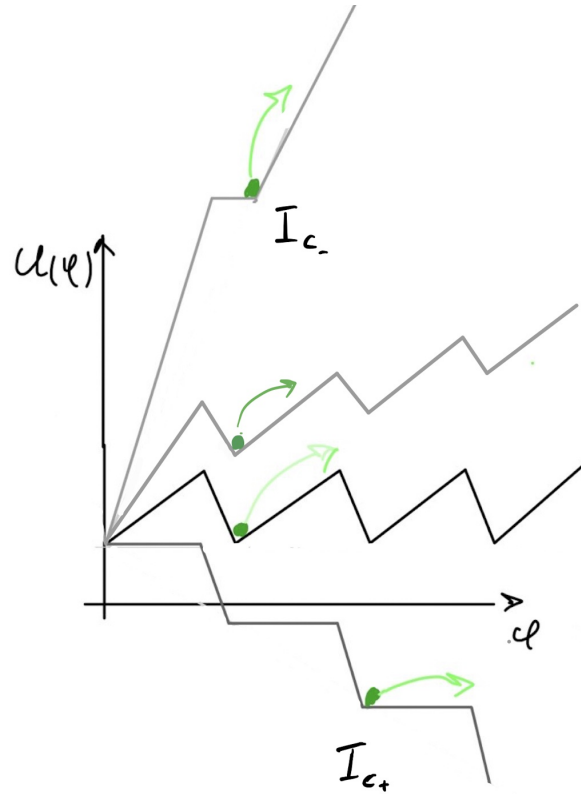


Figure 2.4: A ratchet potential for $I_{dc} = 0, I_{c-}, I_{c+}$.

If the countercurrent becomes too large, the ratchet stops. We refer to such a current as the stopping current or stopping force. As illustrated in Fig. 2.4, if the ratchet transport initially occurs in the positive direction along the φ -axis, we apply $I_{dc} < 0$. This results in a potential tilt of $-I_{dc} \cdot \varphi$, allowing the particle can still climb due to the ratchet effect and perform some useful works.

The rectification curve for a loaded ratchet is schematically depicted in Fig. 2.5.

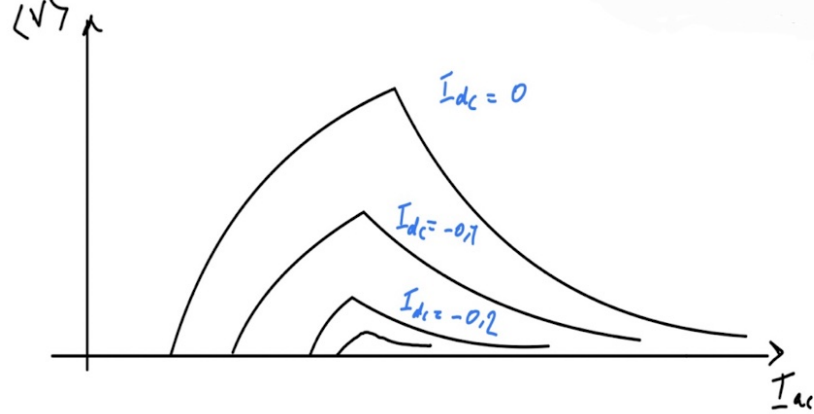


Figure 2.5: The schematic loaded ratchet up to countercurrent $|I_{dc}| = 0.2 \mu\text{A}$.

It is evident that gradually increasing the load $|I_{dc}|$ leads to a reduction in the size of the rectification window and the values of \bar{V}_{dc} . This reduction shows that the ratchet is not strong enough for any I_{ac} . Specifically, we observe that as the load $|I_{dc}|$ increases, the operational range in terms of I_{ac} decreases. However, in this narrower interval, the particle is compelled to move against the ratchet motion and produce more useful power. Our primary objective is to maximize both the rectification windows (RWs) and the value of the stopping current.

To summarize this section, let us consider an example simulation of a ratchet³ that was studied in [1] and [4]. The simulations were conducted in a quasistatic regime, allowing for the acquisition of information about the ratchet's operation solely from its asymmetric IVC. The authors generated a step-like asymmetric IVC, as shown in Fig. 2.6(a), and simulated various figures of merit based on this asymmetric IVC. Fig. 2.6(b) presents the simulation results for a loaded rectification curve \bar{V}_{dc} .

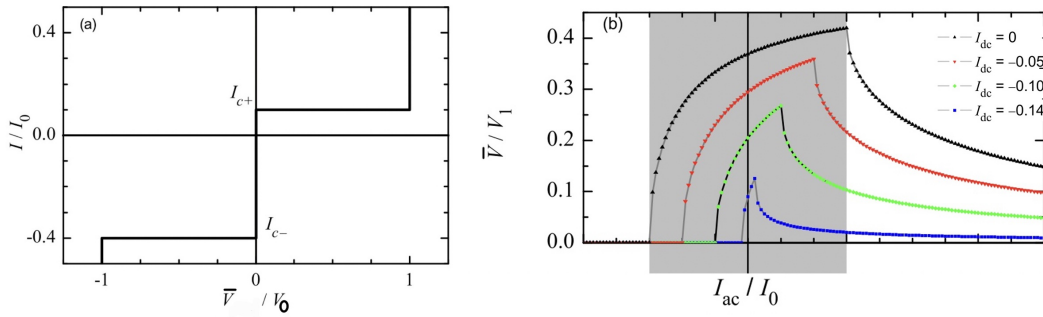


Figure 2.6: (a) A custom-made asymmetric IVC with $\mathcal{A} = 4$. (b) The rectification curves for several values of I_{dc} based on the asymmetric IVC, borrowed from [1].

³A deterministic underdamped Josephson vortex ratchet consisting of a long Josephson junction with $L \geq \lambda_J$.

The black curves in Fig. 2.6(b) correspond to the case where $\mathcal{A} = 4$ and $I_{dc} = 0$. By loading the ratchet and increasing I_{dc} (colored curves), we observe that the rectification window (RW) becomes shorter. Consequently, the asymmetry parameter is reduced⁴. However, within this shorter interval, the particle can perform more useful work and achieve higher efficiency, as we will explain in the following subsection.

2.1.2 Efficiency

Efficiency is defined as useful output dc power \bar{P}_{out} divided by the total input power consumed by the system \bar{P}_{in}

$$\eta \equiv \frac{-\bar{P}_{out}}{\bar{P}_{in}}. \quad (2.2)$$

As a case study, the efficiency of the model investigated in [1] is presented in Fig. 2.7(e). The black curve represents the idle ratchet, while the colored curves correspond to loaded ratchets with different values of $|I_{dc}|$. From Fig. 2.7(c), we observe that as I_{ac} increases, the input power \bar{P}_{in} also increases, reaching its maximum at the end of the rectification window (RW). The ratchet operates with maximum efficiency η at the beginning of the RW for any stopping force, as shown in Fig. 2.7(e). Furthermore, we notice that increasing $|I_{dc}|$ results in a shorter operation interval but a higher efficiency. In [4], it was demonstrated that the maximum efficiency achievable in principle is determined solely by the asymmetry of the potential, given by $\eta_{max} = \frac{I_{c_-} - I_{c_+}}{I_{c_-} + I_{c_+}}$. Overall, we can observe that a higher asymmetry leads to a higher maximum efficiency.

⁴To see this, one can express the asymmetry parameter in terms of the rectification window as $\mathcal{A} = \frac{I_{c_+} + \Delta}{I_{c_+}}$, making it clear that decreasing Δ leads to a reduction in asymmetry.

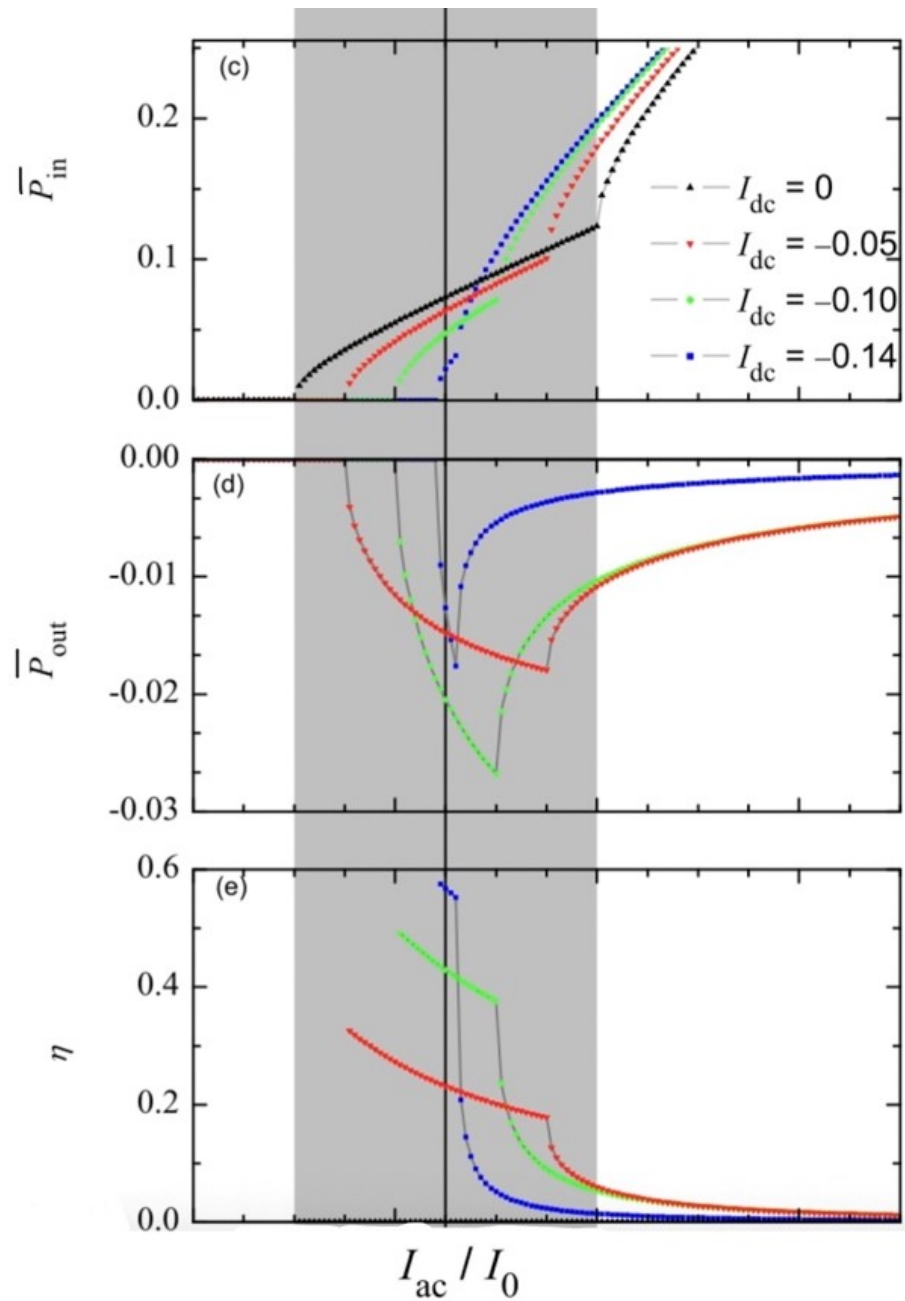


Figure 2.7: (c) Average input ac power \bar{P}_{in} . (d) Average output dc power \bar{P}_{out} . (e) Efficiency η , fig(4) of [1].

2.1.3 Junctions of In-line Geometry

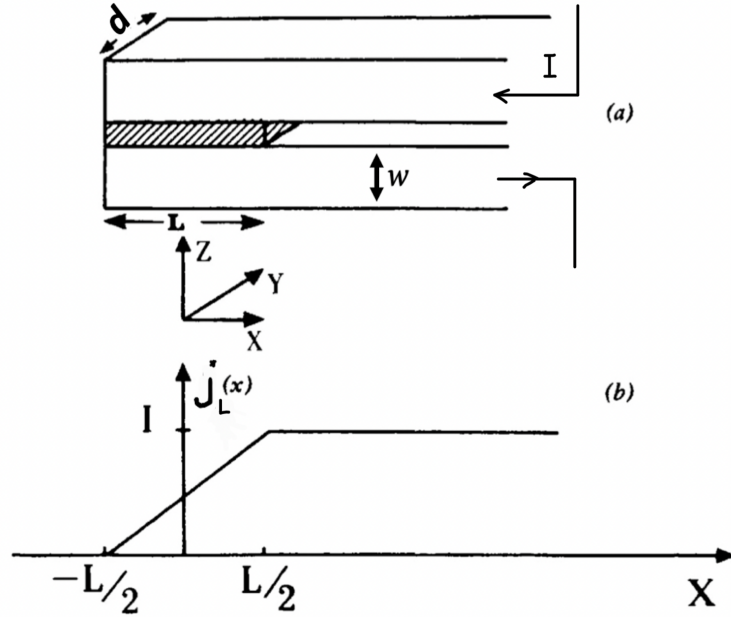


Figure 2.8: (a) The in-line geometry of a (JJ) consists of superconducting where the dashed line represents the barrier JJ surrounded by superconductors. The arrows indicate the current I flowing through the superconductors. (b) The current density j_L as a function of distance x .

In the classical textbook on the Josephson effect [8], Barone *et al.* considered an in-line JJ geometry, as shown in Fig. 2.8(a). In this geometry, the bias current fed from the right side flows through the Josephson barrier (the dashed hatched region) and produces the so-called self-field. We assume that the maximum supercurrent corresponds to the uniform current flow across the Josephson barrier with the current density j_{c0} . By solving the continuity equation $\left(\partial_x \left(\frac{I_L}{d}\right) = j_{c0}\right)$ with the boundary conditions $I_L(-L/2) = 0$ and $I_L(L/2) = I_0$, we obtain the current through the top electrode as

$$I_L(x) = j_{c0}d \left(x + \frac{L}{2} \right).$$

By solving Maxwell equation $\vec{\nabla} \times H_s = j_L(x)$, where $j_L(x) = I_L(x)/(wd)$, we obtain

$$H_s(x) = \frac{j_{c0}}{w} \left(\frac{x^2}{2} + \frac{Lx}{2} \right).$$

Following [8], we substitute this field profile by its average value

$$\overline{H}_s = \frac{5j_{c0}L^2}{12w} = \frac{5I_0L}{12wd}, \quad (2.3)$$

which represents the self-field when we apply the maximum supercurrent $I = I_0$ through the junction. If we apply arbitrary I , then the self-field is given by $\bar{H}_s(I) = \bar{H}_s I / I_0$. The self-field together with the applied external magnetic field H_e , $H = H_e + H_s$ skews $I_c(H)$, as shown in Fig. 2.9. The maximum Josephson current through Josephson junctions is given by (see eq. (5.1.4) of the book [8])

$$I(H_e) = dLj_{c0} \left| \frac{\sin \left(\frac{\mu_0 \pi d_{\text{eff}} L}{\Phi_0} H \right)}{\left(\frac{\mu_0 \pi d_{\text{eff}} L}{\Phi_0} H \right)} \right|, \quad (2.4)$$

for small junction compared to Josephson penetration depth. One can rewrite the eq. (2.4) in terms of normalized fluxes as follows

$$\frac{I_c(f)}{I_0} = \left| \frac{\sin \pi \left(f + f^M \frac{I_c(f)}{I_0} \right)}{\pi \left(f + f^M \frac{I_c(f)}{I_0} \right)} \right|, \quad (2.5)$$

where $I_0 = dLj_{c0}$ is the maximum value of supercurrent I . We have defined normalized flux $f \equiv \Phi_J/\Phi_0$, where $\Phi_J = d_{\text{eff}} L H_e$ is the total applied flux inside JJ. The length of the JJ is denoted by L , and the effective magnetic thickness d_{eff} is given by $d_{\text{eff}} = 2\lambda_{\text{eff}} \tanh(w/\lambda_{\text{eff}})$. Here, λ_{eff} is the effective London penetration depth, defined as $\lambda_{\text{eff}} = \lambda \coth(d/\lambda)$, where λ is the London penetration depth.

It is important to note that the Josephson penetration depth for the in-line geometry in this case differs from the eq. (1.15) in terms of magnetic thickness for the geometry shown in Fig. 2.8. The Josephson penetration depth for the in-line geometry is defined as

$$\lambda_J \equiv \left(\frac{\Phi_0}{2\pi\mu_0 d' j_{c0}} \right)^{1/2},$$

where $d' \mu_0$ is called specific inductance of electrode, and $d' = 2\lambda_{\text{eff}} \coth(w/\lambda_{\text{eff}})$ for our in-line geometry. Additionally, we introduce $f^M \equiv \Phi_s^M / \Phi_0$ as the geometric normalized flux, where Φ_s^M describes the strength of the in-line geometry. It is determined by the eq. (2.4), and the definition of the self-field given in eq. (2.3), as follows

$$\Phi_s^M = \mu_0 \bar{H}_s d_{\text{eff}} L = \frac{5\mu_0 L^2 d_{\text{eff}} I_0}{12dw}. \quad (2.6)$$

Φ_s^M describes how much the $I_c(H)$ plot is skewed and deviated from the symmetric dependence as shown in Fig. 2.9. We can express f^M in terms of the Josephson penetration depth λ_J using the following equation

$$f^M = \frac{5L^3 d_{\text{eff}}}{24\pi\lambda_J^2 w d'}. \quad (2.7)$$

At $f^M = 0$, the maximum supercurrent $I_c(f)$ becomes unskewed and symmetric, following the Fraunhofer pattern $I(f) = I(-f)$ as given by the eq. (1.20) as shown in Fig. 1.5. Eq. (2.5) defines an implicit function of I on the flux f , which requires numerical solutions. We have developed a Python script that uses the bisection method to solve eq. (2.5) numerically. The script calculates $I_c(f)$ for several fixed values of f^M and is depicted in Fig. 2.9. One can see the skewness of $I_c(f)$ depends on f^M . Visually, if we draw a vertical line at a fixed value of f , it becomes evident that $|I_{c+}| \neq |I_{c-}|$ for most of the f values. Therefore, we can quantify the degree of skewness using the asymmetry parameter \mathcal{A} .

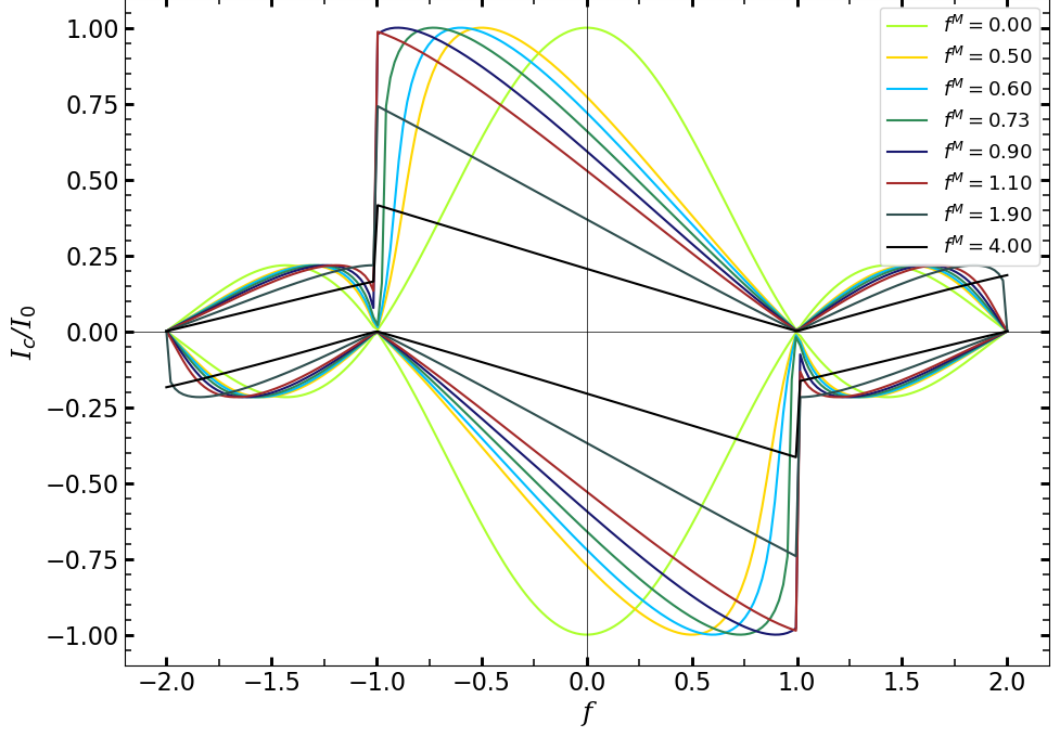


Figure 2.9: A family of asymmetric $I_c(f)$ for different f^M obtained by solving the eq. (2.4) numerically.

Note that the maximum asymmetry at the optimum point f_{opt} (where the asymmetry is maximum) of f is symmetric under changing the sign of f . Now let's examine the behavior of \mathcal{A} as a function of f for different values of f^M . In Fig. 2.10(a), we can observe the dependence of the asymmetry parameter \mathcal{A} on f for various fixed values of f^M . For instance, for the blue curve ($f^M = 0.6$), we find that the asymmetry parameter $\mathcal{A} \approx 8$ at the optimum value of $f_{\text{opt}} \approx -0.9$. This maximum asymmetry value increases as the value of f^M increases. In Fig. 2.10(b), we present the dependence of the maximum asymmetry $\mathcal{A}_{\max}(f^M)$ at the optimum value of f . One can see from both Fig. 2.10(a) and 2.10(b) that \mathcal{A} increases with increasing f^M .

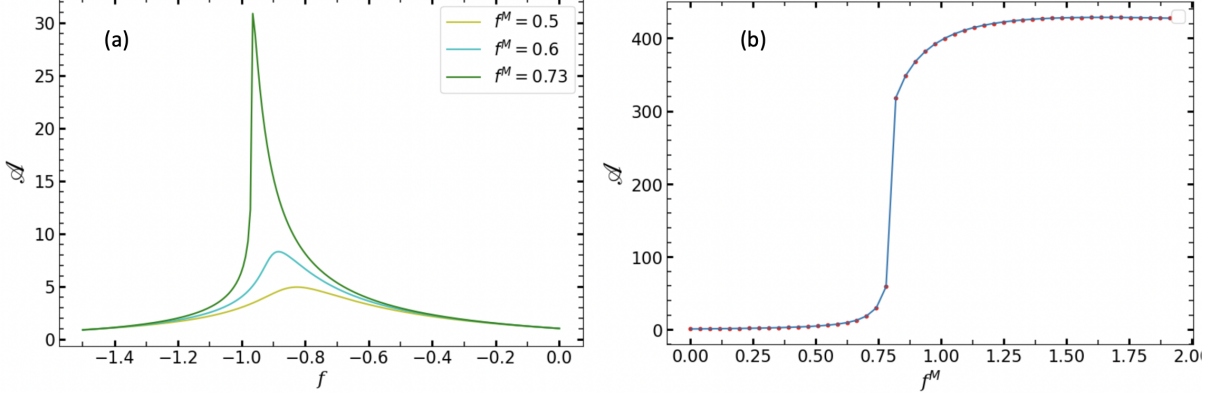


Figure 2.10: (a) Asymmetry parameter \mathcal{A} vs. magnetic flux f for different values of f^M . (b) Asymmetry parameter \mathcal{A} vs. strength of in-line geometry f^M .

Thus, using in-line JJs and the appropriate applied normalized flux f , one is able to design a Josephson ratchet with a high asymmetry parameter. It is important to emphasize that the maximum asymmetry achieved at f_{opt} for the curve with a high value of f^M exceeds 100, as shown in Fig. 2.10(b). This happens because from some optimum points (for example around $f^M \approx 0.9$) onward we observe that increasing the value of f^M does not alter the optimum point, see Fig. 2.9. Instead, one of the critical currents, specifically I_{c+} in our case, tends to approach zero at a faster rate compared to the other one (I_{c-}). Consequently, this leads to a divergence of the asymmetry parameter, approaching infinity as defined. However, it should be noted that achieving such high asymmetry in experiments is not feasible. In reality, the system is subjected to substantial amounts of noise affecting the amplitude of $|I_{c\pm}|$, especially near the critical points, where $|I_{c\pm}|$ should approach zero. This substantial noise leads to a substantial reduction in the actual asymmetry parameter compared to the intended target parameter. Therefore, achieving extremely high asymmetry values as theoretically predicted is challenging in experimental settings.

In the next chapters, we will examine these challenges as well as the optimal target parameters for designing an effective Josephson ratchet. This will be done once we are prepared to commence the ratchet implementation.

Chapter 3

Fabrication and Implementation

3.1 Sample Information

The sample was prepared using a commercial YBCO thin film produced by a company named Ceraco. The sample was deposited layer by layer on a 2-inch LSAT substrate, starting with a buffer layer of cerium oxide (CeO), followed by a 30 nm $\text{YBa}_2\text{Cu}_3\text{O}_7$ (YBCO) film, and finally, a 20 nm layer of gold (Au) was deposited on top, as shown in Fig. 3.1(b). The detail information of the chip is provided by the company, as shown in Fig. 3.1(a).

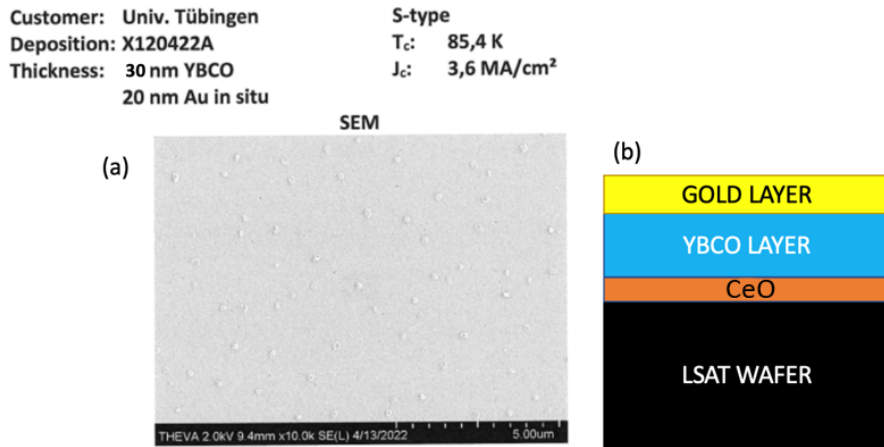


Figure 3.1: YBCO film on 2 inch LSAT substrate. (a) The scanning electron microscope picture of the sample surface. The critical temperature T_c and the value of the current density j_c are provided by Ceraco. (b) A schematic picture of the chip showing the deposition of its different layers.

3.2 Sample Layout

The general layout of the sample is shown in Fig. 3.2. It consists of two columns of 18 bridges, making a total of 36 bridges. Each bridge has two contact pads on one

side, and all the bridges are connected to the main central lines (vertical in Fig. 3.2), which is also connected to two ground pads on both sides.

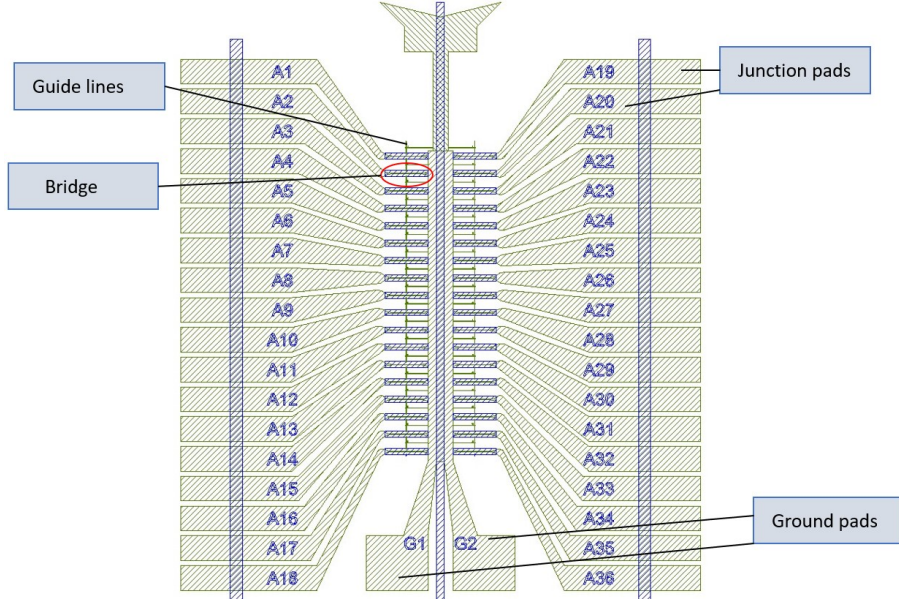


Figure 3.2: The layout of the sample. The hatched light green areas correspond YBCO covered by Au, while the blue areas represent Au removal mask down to YBCO. The guide lines are also covered by Au. The Au layer is removed down to YBCO on the bridges, and two separate pads onto two parts for I & V .

3.3 Sample Fabrication

The first step of the fabrication process involves dicing the 2 inches film into $1 \times 1 \text{ cm}^2$ chips. These pieces are then cleaned using an ultrasound bath filled with acetone, followed by two rounds of cleaning with isopropanol in an ultrasound bath. After dicing and cleaning, the sample is spin-coated with a photoresist called “ma-P1205” and later dried on a hotplate at 90° Celsius for 210 seconds. The chip is then placed into a maskless aligner model for the patterning process, which consists of two steps.

(i). Etching of the gold: Once the chip is inside the maskless aligner, a laser beam scans the patterned layout as shown in Fig. 3.3(a), which modifies the properties of the photoresist. The chip is then removed from the machine, and the modified photoresist is developed using “ma-D 331/S” for 50 seconds. It is quickly transferred to water to wash away the excess developer, and then transferred to another flask with water for further cleaning. The sample is then dried, and the gold is etched using an Argon ion beam. After the etching process is completed, the remaining photoresist is removed, and the chip is spin-coated again under the same mentioned conditions.

(ii). Etching of the YBCO: The chip is once again loaded into the maskless aligner to proceed with the second etching step. The same process as in step **(i)** is carried out, but this time the machine scans another mask, as shown in Fig. 3.3(b).

The photoresist is modified again, and after removing the chip from the maskless aligner, it is selectively developed with “ma-D 331/S” and rinsed in water twice. Then, it is dried again, and the YBCO is etched with H_3PO_4 0,1%. After the etching process, the remaining photoresist is removed once again, and the chip is ready to be diced once more.

A $1 \times 1 \text{ cm}^2$ chip is divided into four similar smaller chips of $5 \times 5 \text{ mm}^2$. Each small chip is labeled with a letter: A, B, C, and D. Each of them can accommodate 36 JJ. [10] Zoom-in pictures of the bridges after each step of etching are shown in Fig. 3.4.

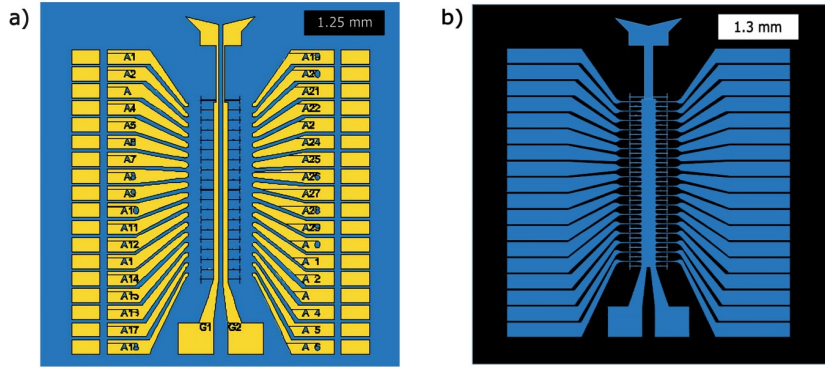


Figure 3.3: Masks used during the patterned process: (a) Mask used during step (i) for the etching of gold. The blue zone indicates where the gold has been removed, leaving only YBCO. The yellow zones indicate where the gold still remains. (b) The mask used during step (ii) for the etching of YBCO. The areas in blue represent the regions where the YBCO still remains. The black area represents LSAT (substrate). Note that in the regions where the gold remains from the first step (e.g., over the pads), it has not been removed during the second step.

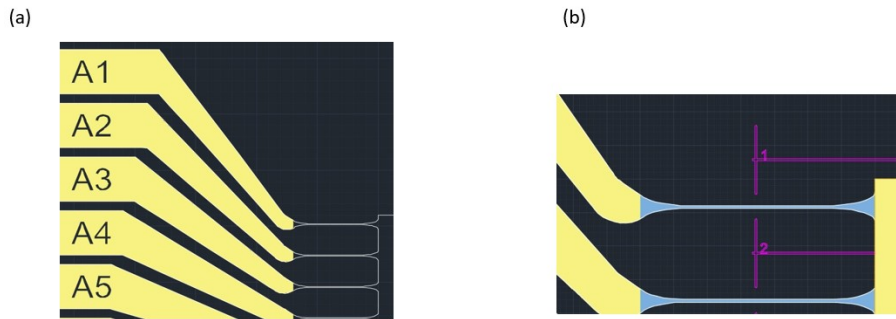


Figure 3.4: The microscope pictures of the sample after each step of the lithography process: (a) Picture of the pads after the step (i). The dark areas represent YBCO, and the yellow areas represent gold. (b) The picture of the bridges after the step (ii). The yellow area represents gold, the dark area represents LSAT, the blue area represents YBCO where the junction will be finally irradiated, and the purple lines are guide lines for our next step using He-FIB.

We are now prepared to bring the sample to the Helium ion beam (He-FIB) laboratory in order to produce JJs and Josephson ratchets using the Focused Helium Ion Beam.

3.4 He-FIB

We utilize a He-FIB system with an energy of 30 keV to fabricate the Josephson barrier and create the BJJ (Barrier Josephson Junction). The process is illustrated in Fig. 3.5, which provides a concise overview of the He-FIB technique.

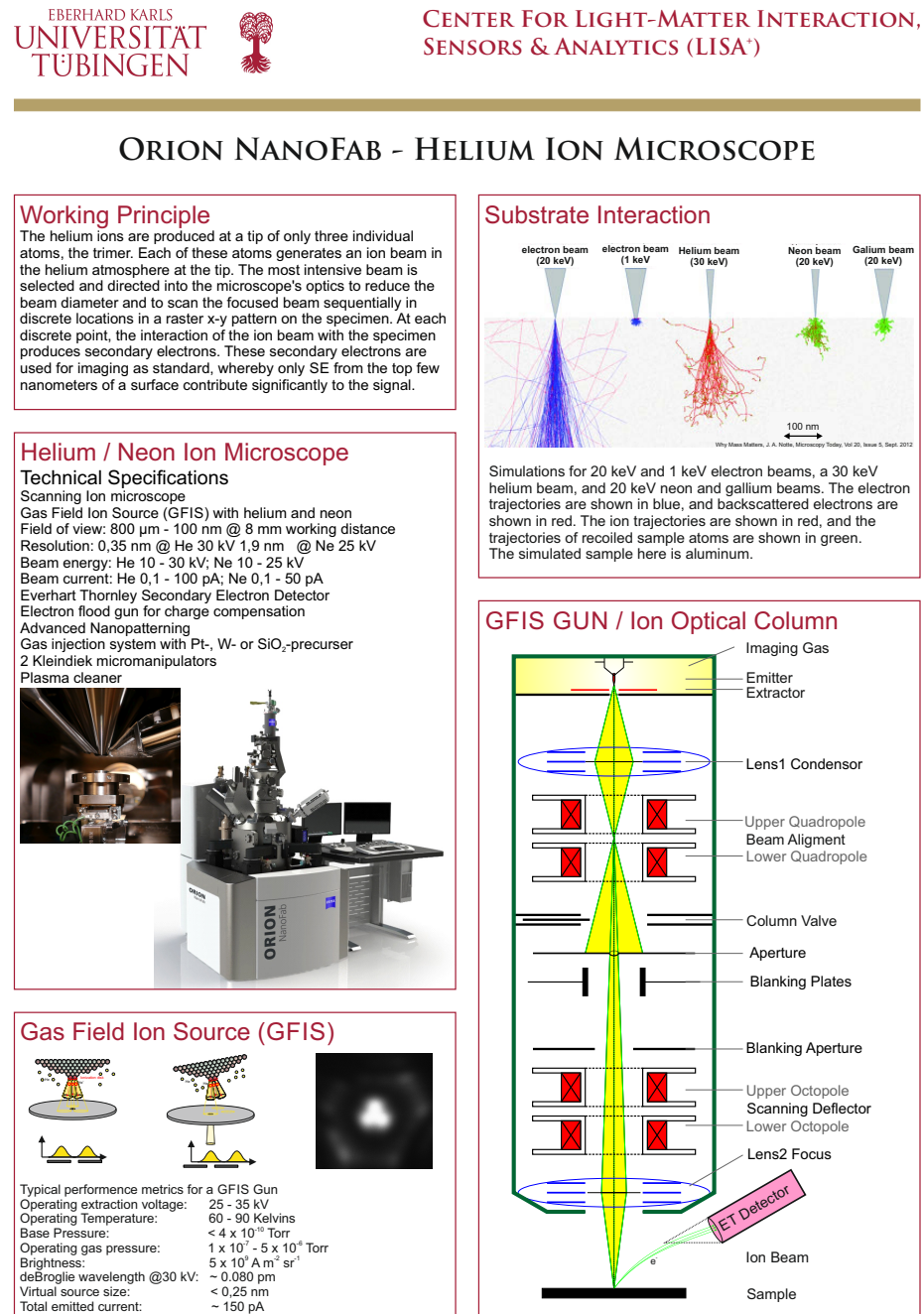


Figure 3.5: The poster of He-FIB.

The schematic illustration of producing BJJ using He-FIB is shown in Fig. 3.6. We create the Josephson barrier by irradiating the bridge a long the line with a certain dose D (ions/nm). The helium ions create either a very thin (few nm) amorphous region or a line (also a few nm wide) that suppresses T_c (changes doping), thus acting as the barrier Josephson junction between two superconductors. In [11], it was experimentally shown that the critical current density j_c of the resulting BJJ depends on the irradiation dose D approximately as

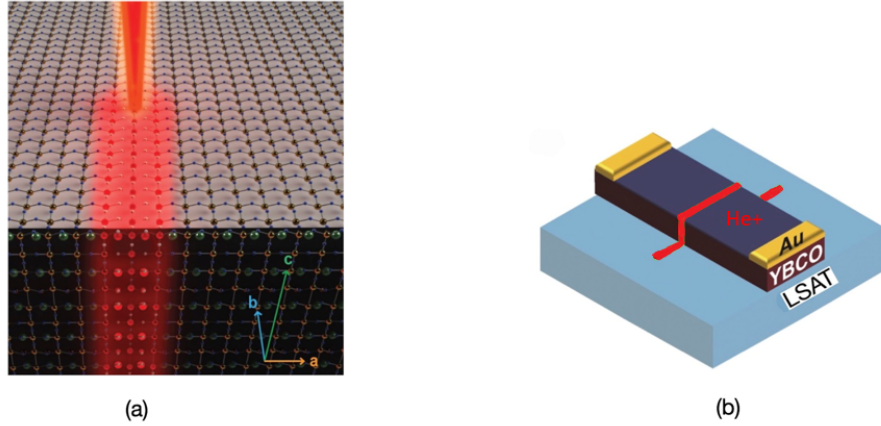


Figure 3.6: (a) The red line indicates focused He ion beam on the atomic level with a width of the order of a few nm. (b) Schematic sketch of the BJJ produced by He-FIB, where the red line indicates the barrier JJ.

$$j_c(D) \approx j_{c0} \exp(-D/D_0), \quad (3.1)$$

where j_{c0} (A/cm^2) and D_0 (ions/nm) are the critical current density at $D = 0$ and the characteristic dose, respectively. They can be obtained by fitting experimental data using eq. (3.1).

The BJs made by He-FIB can be changed continuously from a conducting to a completely insulating state by varying the irradiation dose. In fact, high-dose He-FIB irradiation disturbs the internal atomic structure of YBCO, making the irradiated line amorphous and highly resistive. It can effectively act as a resistive wall with $j_c = 0$. We utilize this technique to fabricate Josephson ratchets with more complex geometries than BJs (see, for example, Fig. 3.12).

3.5 Characterization

Before implementing the ratchet, we conducted a characterization of a series of BJs with varying doses to determine the values of j_{c0} and D_0 for our specific chip. We fabricated 11 BJs with dose series ranging between 450...700 ions/nm and subsequently measured the critical current of each junction. The results are presented Table. 3.1

BJJs	Dose (ions/nm)	Maximum I_c (μA)
D19	455	15.6
D20	455	13.2
D21	505	11.5
D22	505	6.8
D23	556	1
D24	556	3.7
D25	606	1.4
D26	606	0.59
D27	657	0.17
D28	657	0.79
D29	707	0.29

Table 3.1: The maximum I_c is determined by measuring $I_c(H)$ and selecting the highest value.

Next, we wrote a short Python script to fit the experimental data using eq. (3.1) with j_{c0} and D_0 as fitting parameters. The result is shown in Fig. 3.7.

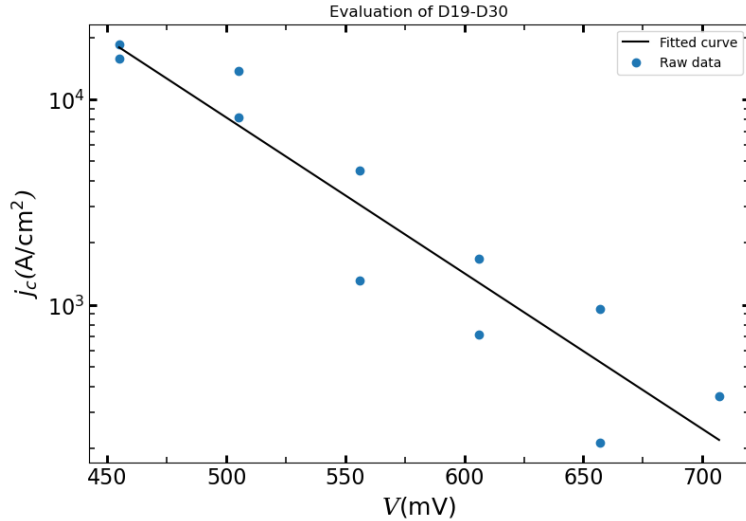


Figure 3.7: Experimental measured $j_c(D)$ (symbols) and fit (line). In total, eleven BJJs measured with the dose $D \approx 450\ldots700$ ions/nm. The width of the BJJs is $W = 2.8 \mu\text{m}$.

As a result of fitting, we obtained $j_{c0} \approx 5 \times 10^7 \text{ A}/\text{cm}^2$ and $D_0 = 57.2$ ions/nm. As an example, we present IVC and $I_c(H)$ of several BJJs in Fig. 3.8 to Fig. 3.11.

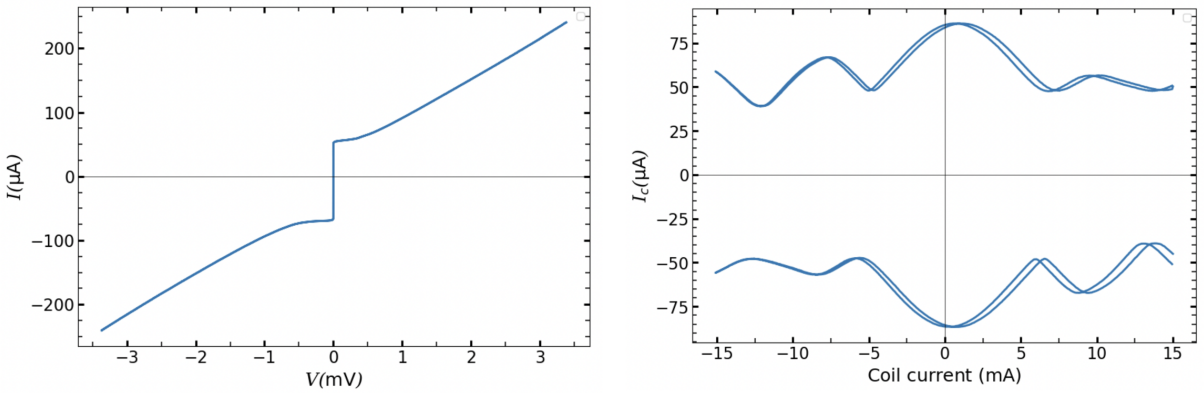


Figure 3.8: IVC and $I_c(H)$ of junction B28 with $D = 350$ ions/nm.

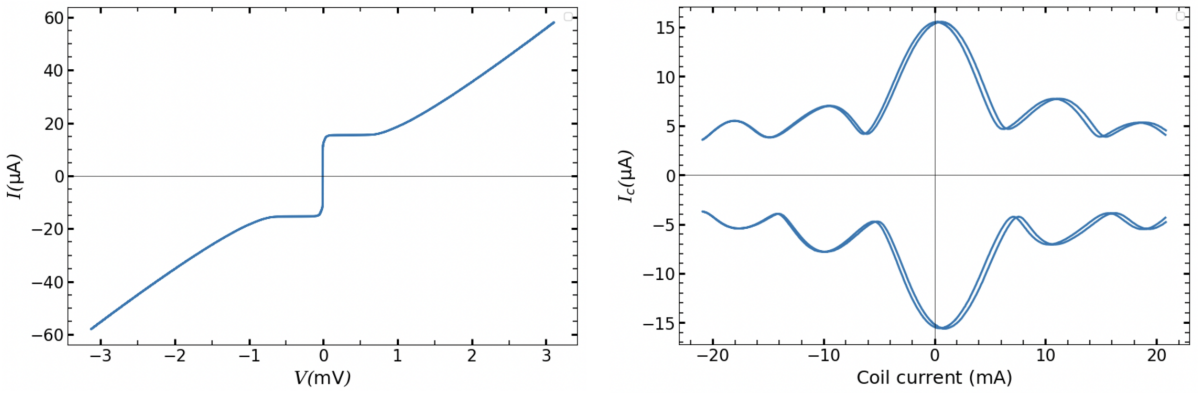


Figure 3.9: IVC and $I_c(H)$ of junction D19 with dose $D = 450$ ions/nm.

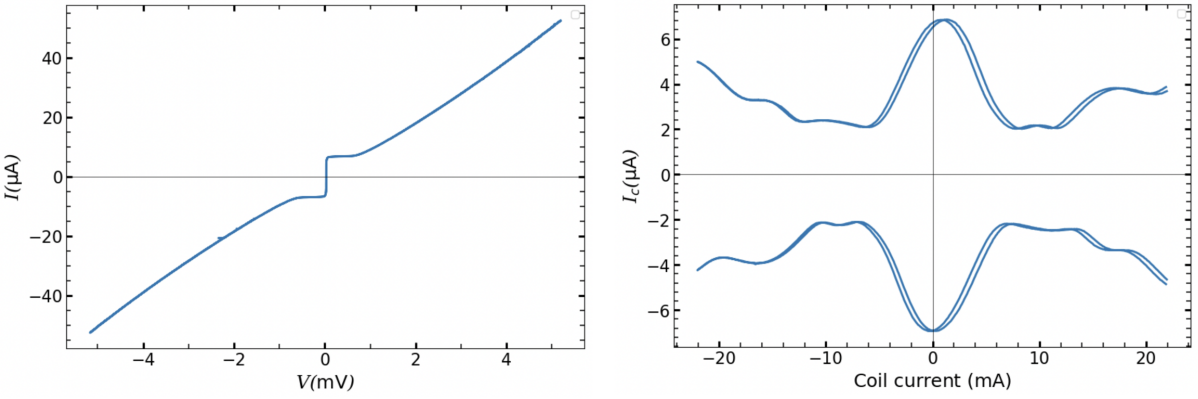


Figure 3.10: IVC and $I_c(H)$ of junction D22 with dose $D = 505$ ions/nm.

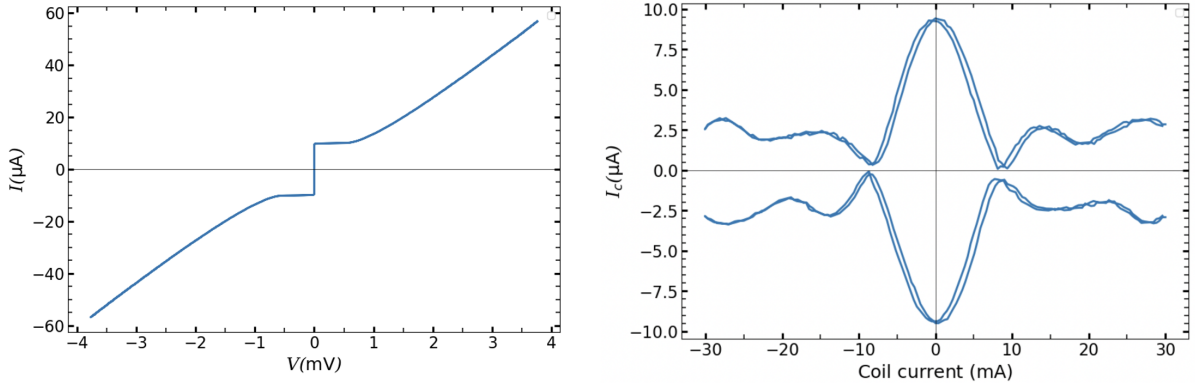


Figure 3.11: IVC and $I_c(H)$ of junction B33 with dose $D = 600$ ions/nm.

3.6 Implementation of an In-line Geometry Josephson Ratchet

In-line geometry

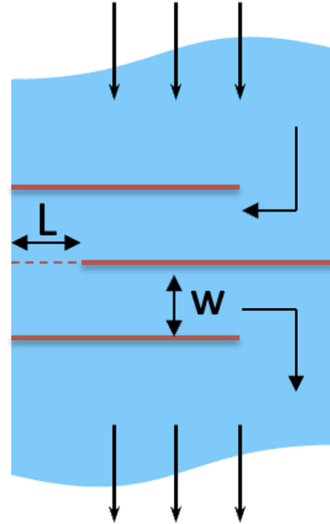


Figure 3.12: Sketch of the Josephson ratchet. The blue zone is YBCO, the red solid lines are the resistive walls, dash red line is the BJJ, and arrows indicate the flow of the supercurrent through the Josephson ratchet. w is the distance between two resistive walls and L is the length of BJJ.

In the Chapter 2.1.3, we explored the impact of the in-line geometry of a JJ on the generation of a self-field within our device. This field is characterized by f^M , which is described by the eq. (2.7). Additionally, we examined how this parameter influences the skewness of $I_c(H)$ and, consequently, the asymmetry parameter.

In this master thesis, we focus on the implementation of a highly efficient ratchet based on reasonable theoretical parameters. For instance, eq. (2.7) clearly demonstrates the geometric dependencies of the f^M on the length L of JJ and w . Therefore, we would design the ratchets with various values of f^M , while varying the length L of the JJ through definition of f^M in eq. (2.7).

To optimize the distance between the two resistive walls w , we must avoid making it too small (e.g., less than or equal to 100 nm) to prevent the destruction of the crystal configuration of YBCO due to the resistive walls. Moreover, extremely small values of w can lead to the emergence of topological defects. Throughout this work, we refrain from reducing w below 200 nm.

Hence, our target parameters are selected as follows: after determining the desired value of the dimensionless parameter f^M , we choose the necessary supercurrent density $j_c(D)$ by adjusting the He-FIB according to the eq. (3.1). From the value of j_c , we calculate the Josephson penetration depth λ_J and determine the appropriate length L using eq. (2.7). Knowing j_c we can find the critical current by $I_c = j_c \cdot L \cdot d$, where in our case, $d = 30$ nm. It is important to mention that the expression for the Josephson penetration depth given by λ_J can be written to show the effect of the inductance of superconducting electrodes explicitly as

$$\lambda_J^K = \sqrt{\frac{\Phi_0 L}{2\pi j_c 2L_K d}}, \quad (3.2)$$

where $L_K = \mu_0 \lambda^2 \frac{L}{w \cdot d}$ is the kinetic inductance. Substituting L_K into the eq. (3.2) gives us

$$\lambda_J^K = \sqrt{\frac{\Phi_0 w}{4\pi \mu_0 j_c \lambda^2}}. \quad (3.3)$$

Next, similar to the Chapter 2.1.3, we can write f_K^M with respect to the λ_J^K as

$$f_K^M = \frac{5L^3 d_{\text{eff}}}{24\pi(\lambda_J^K)^2 w d'}, \quad (3.4)$$

where $d' = 2\lambda \coth(w/\lambda)$.

In Table. 3.2, we present two sets of target parameters for the ratchets A15 and A22, which will be discussed in detail later.

Target Parameters	A15	A22
$w(\text{nm})$	300	200
$D(\text{ions/nm})$	507	531
$j_c (\text{kA/cm}^2)$	7.15	4.8
$I_c(\mu\text{A})$	3.8	2.5
$\lambda_J(\text{nm})$	250	250
$L(\text{nm})$	1750	1750
$l \equiv L/\lambda_J$	7	7
f^M	0.25	0.26
$\lambda_J^K(\text{nm})$	2960	2960
$l_K \equiv L/\lambda_J^K$	0.6	0.6
f_K^M	0.09	0.1

Table 3.2: Comparison table of target parameters between ratchet A15 and A22.

Chapter 4

Experimental Results

4.1 An Overview

In this chapter, we report a set of experimental results for the ratchets A22 and A15. First, we compare the actual (experimental) and target (theoretical) parameters of each devices. Then we present our experimental data, including IVC, $I_c(H)$, \bar{V}_{dc} , \bar{P}_{out} , \bar{P}_{in} , and, finally, the efficiency η . Afterward, we compare our experimental results with their simulations in the quasistatic regime. Finally, we drive our system with stochastic drive and investigate the effect of different types of noises, such as external and internal noises plus possibly some other sources. It is shown that internal noise, e.g., thermal noise sources, can be rectified into the output dc voltage.

4.2 Josephson Ratchet A22

In Table 4.1, the actual and target parameters of the device A22 are presented.

A22	Target parameter	Actual parameter
$w(\text{nm})$	200	200
$D(\text{ions/nm})$	531	531
$j_c (\text{kA/cm}^2)$	4.8	28
$I_c(\mu\text{A})$	2.5	14.8
$\lambda_J(\text{nm})$	250	103
$L(\text{nm})$	1750	1750
$l_j \equiv L/\lambda_J$	7	17
f^M	0.26	1.54
$\lambda_J^K(\text{nm})$	2960	1220
$l_K \equiv L/\lambda_J^K$	0.6	1.4
f_K^M	0.1	0.63

Table 4.1: Comparison table of target and actual parameters of ratchet A22. Notice that we chose $\lambda = 250 \text{ nm}$ and subsequently $\lambda_{\text{eff}} = 2 \mu\text{m}$.

In general, discrepancies between the actual and target parameters can arise due to various factors, such as fabrication techniques, lithography processes, and the accuracy of I_c measurements. The dose D has a fairly precise value of around two percent.

Since the precision of He-FIB is on the scale of a few nanometers, our geometric parameters, such as length L and w , are also quite accurate. According to eq. (3.1), the value of j_c has an exponential dependence on the dose, and the spread is quite high, which is typical for our technology. Consequently, I_c , λ_J , the normalized length l_j , and f^M follow from their definitions and dependencies on the actual j_c .

Since we are working in the thin film limit, where $d \ll \lambda$, our $\lambda_{\text{eff}} = \frac{\lambda^2}{d} = 2 \mu\text{m}$, as we defined in the section. 2.1.3. In this limit, the contribution of kinetic inductance becomes dominant. Therefore, we should consider the effect of the inductance on the Josephson penetration depth as $\lambda_J^K = 2.9 \mu\text{m}$, which is comparable to λ_{eff} . Thus, the phase $\varphi(t, \mathbf{x})$ in our JJ is described by the non-local model. [12] To our knowledge, the dependency of $I_c(B)$ in the in-line geometry for non-local JJ has not been solved in the literature. Therefore, we use the obtained parameters only as a rough guide, and iteratively investigate many JJ parameters to arrive to a high value of asymmetry.

The IVC of the ratchet A22 is presented in Fig. 4.1.

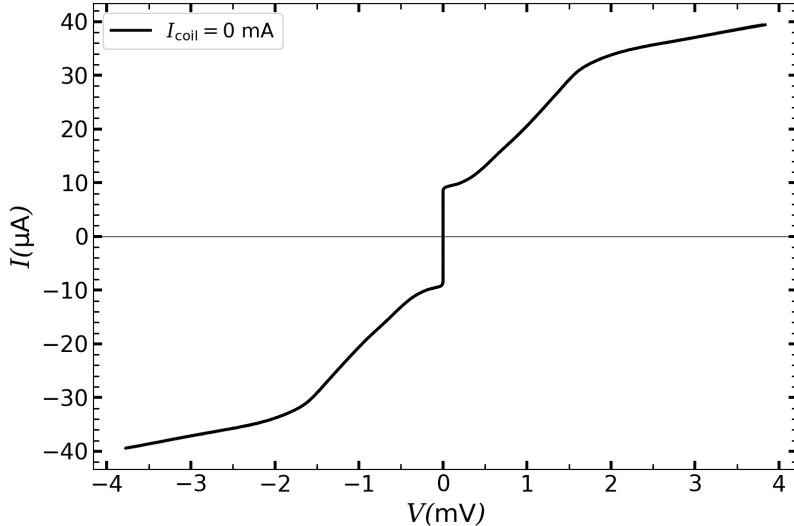


Figure 4.1: IVC of the ratchet A22 at $I_{\text{coil}} = 0$ where $|I_{c+}| \approx |I_{c-}| \approx 8.43 \mu\text{A}$.

The normal resistance R_N of our JJ is $R_N \approx 50 \Omega$, and it is roughly determined by the slope at a current of $I \approx 30 \mu\text{A}$, where the voltage is $V \approx 1.5 \text{ mV}$. It is worth noting that the observed bending near $|I| \approx \pm 32 \mu\text{A}$ may be due to the small distance w between the two resistive walls. As a result, there is a possibility that some crystal destruction of YBCO has occurred in that region, creating a quasi-junction in series with the JJ of the ratchet. This leads a bending of the IVC around $|I| \approx \pm 32 \mu\text{A}$. However, the exact cause cannot be determined with the absolute certainty.

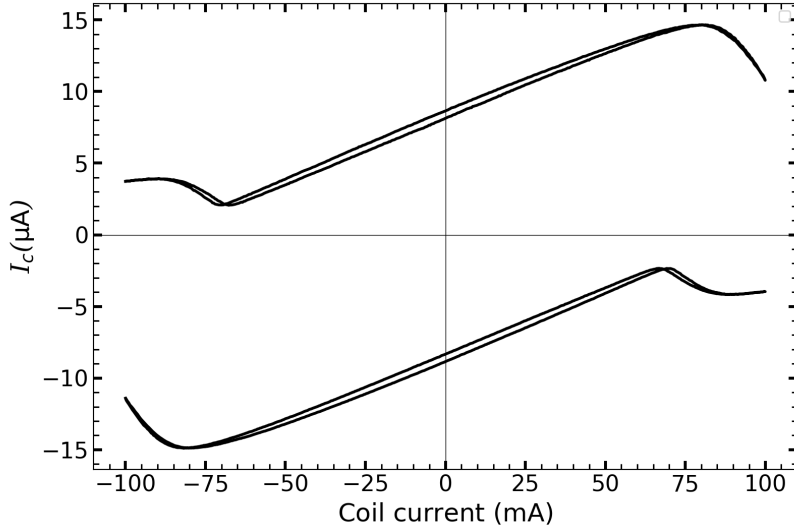


Figure 4.2: Critical current versus magnetic coil current of the Josephson ratchet A22. We used a voltage criterion equal to $1 \mu\text{V}$ for this measurement.

The dependency of $I_{c\pm}(I_{\text{coil}})$ is shown in Fig. 4.2. The coil current I_{coil} generates a magnetic field B perpendicular to the sample plane, and the coil factor we used for our measurement is approximately 0.17 mT . Within our coil current range between $\pm 100 \text{ mA}$, we can clearly observe the skewed nature of $I_c(I_{\text{coil}})$. Using Fig. 4.2, we can identify the optimal magnetic field at which the asymmetry parameter \mathcal{A} reaches its maximum. To observe the dependency of asymmetry parameter (see eq. (2.1)) to the I_{coil} , we have plotted $\mathcal{A}(I_{\text{coil}})$ as shown in Fig. 4.3.

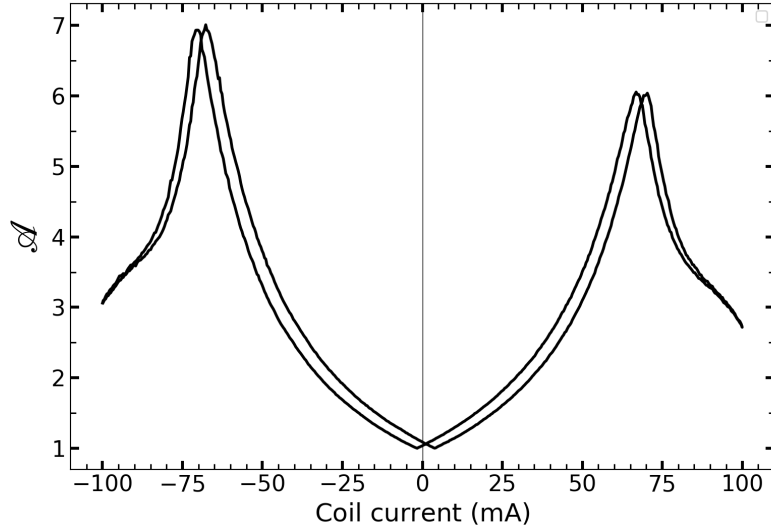


Figure 4.3: The dependency of the value of the asymmetry parameter \mathcal{A} on I_{coil} . The maximum asymmetry, $\mathcal{A} \approx 7$ at the value of $I_{\text{coil}} \approx -69$ mA.

We observe that \mathcal{A} is somewhat asymmetric with respect to the polarity of I_{coil} . For instance, $\mathcal{A}(69 \text{ mA}) \approx 6$ whereas $\mathcal{A}(-69 \text{ mA}) \approx 7$. This asymmetry can be attributed to several factors, such as the shift of zero for the current source used to bias the JJ or the design of our ratchet itself.

Another issue we want to point out concerns the discrepancy between the theoretically predicted \mathcal{A} and the experimental one. As briefly mentioned in page 22, this difference is mainly due to our choice of voltage criterion and various noise sources, such as voltage noises, internal, and external noises, which we will be explained in detail later on in this chapter. These two main reasons cause the I_{c+} at the optimum point in Fig. 4.2 not to be so close to zero as presented theoretically. Therefore, \mathcal{A} is not so close to its theoretical prediction. For example, if we could reduce the thermal and other external source of noises, the I_{c+} in the optimum point ($I_{\text{coil}} \approx -69$ mA) would be much closer to zero and subsequently would make the experimental value of \mathcal{A} much closer to its theoretical prediction. Another possible reason for such a difference is that, e.g., our experimental I_c , see Fig. 4.2, looks qualitatively different from theoretical one Fig. 2.9. For example, the minimum and maximum of I_c in Fig. 2.9 for $f^M > 0.9$ correspond to the same value of coil current, however in the experiment they are not. Therefore, one can expect such a differences of \mathcal{A} in the theory and experiments.

At this point, the important goal for us is to find the optimum I_{coil} where \mathcal{A} has a maximum. Once we have determined the optimum magnetic field, we apply it to our device and measure the IVC, as shown in Fig. 4.4.

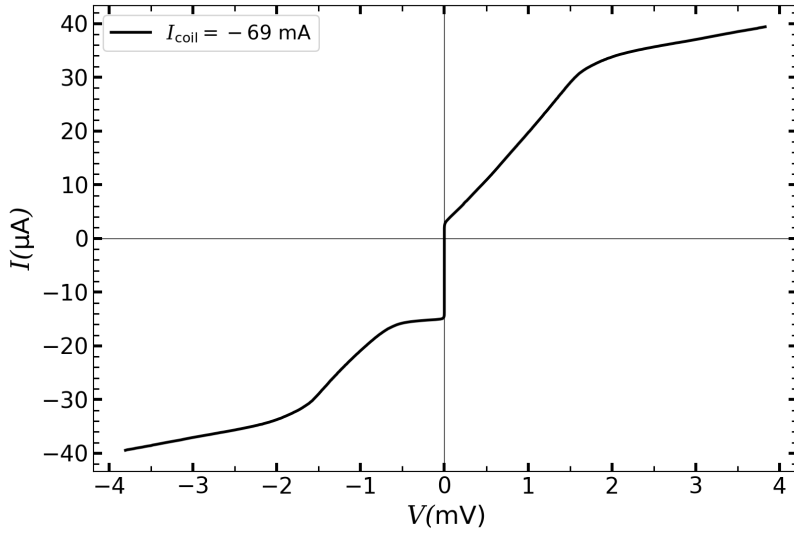


Figure 4.4: The asymmetric IVC of ratchet A22 at the optimum magnetic field (coil current) $I_{\text{coil}} = -69 \text{ mA}$ exhibits $|I_{c+}| \approx 1.53 \mu\text{A}$ and $|I_{c-}| \approx -13.8 \mu\text{A}$, resulting in $\mathcal{A} \approx 7$.

Having such an asymmetric IVC, we can now apply an ac-drive, which is defined by

$$I(t) = I_{\text{ac}} \sin \omega t, \quad (4.1)$$

and measure the rectification curve $\bar{V}_{\text{dc}}(I_{\text{ac}})$, as shown in Fig. 4.5.

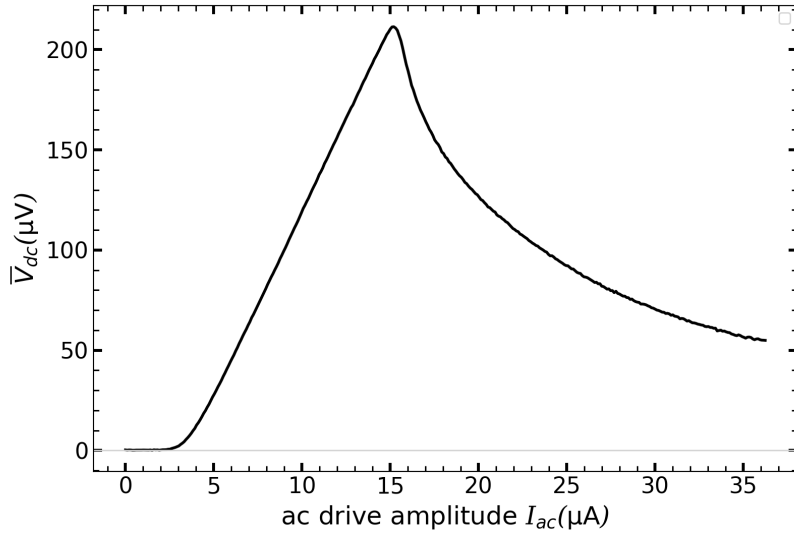


Figure 4.5: The rectification curve for the ratchet A22 at $I_{\text{coil}} = -69 \text{ mA}$, where $|I_{c-}| \approx 15.2 \mu\text{A}$, $|I_{c+}| \approx 2.2 \mu\text{A}$ and RW $\Delta \approx 13 \mu\text{A}$.

For each point, the rectification curve is experimentally measured over 5 ms, which corresponds to one period of the drive.¹ This curve is shown in Fig. 4.5. One can explain the behaviour of $\bar{V}_{dc}(I_{ac})$ using the asymmetric IVC (as shown in Fig. 4.4) as follows. For a small amplitude of ac-drive $I_{ac} < |I_{c_+}|$, V remains zero, so \bar{V}_{dc} remains zero in Fig. 4.5. When the ac-drive amplitude exceeds $|I_{c_+}| \approx 2.2 \mu\text{A}$, the rectification has been occurring. By increasing the amplitude of ac-drive further, the rectification reaches to its maximum average voltage $\bar{V}_{dc} \approx 215 \mu\text{V}$. When the ac-drive amplitude is about to reach $|I_{c_-}| \approx 15.2 \mu\text{A}$, from that point onwards, the average voltage starts decreasing to approach zero.

However, at this stage, our ratchet is still idle. To load it, we apply some counterforce I_{dc} in the opposite direction of the ratchet motion. This force effectively tilts the potential and compels the particle to climb uphill, taking advantage of the ratchet effects and generating useful work. The rectification curves, illustrating the operation of loaded ratchet for different values of I_{dc} , are shown in Fig. 4.6.

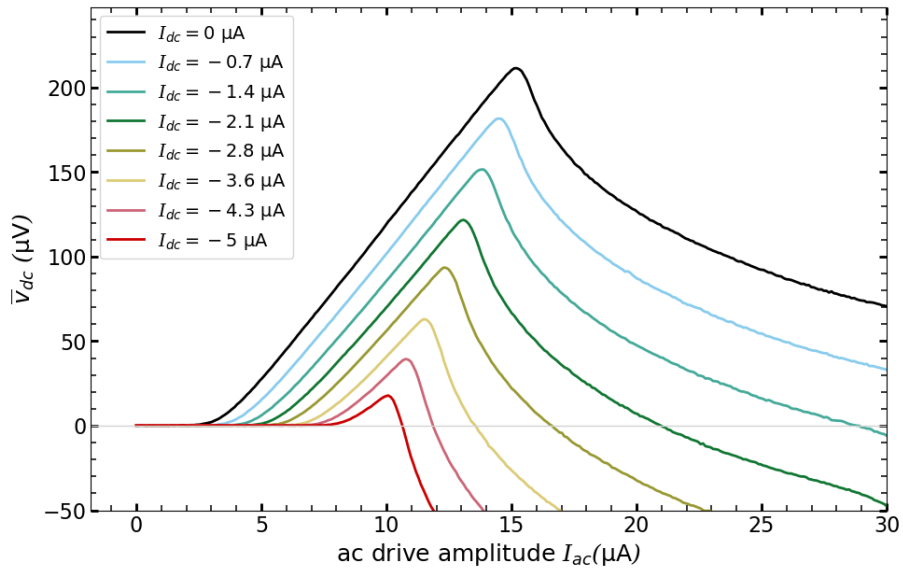


Figure 4.6: The rectification curve for the ratchet A22 at $I_{coil} = -69 \text{ mA}$ for several I_{dc} from 0 (idle ratchet) up to $|I_{dc}| = 5 \mu\text{A}$.

¹For our measurement setup, we employed 500 samples per period and $f = 200 \text{ Hz}$, and so sampling rate equals to $100K$ sample per second.

We observe that as the absolute value of the counterforce increases, the RW gradually decreases until it eventually closes at a stopping force of $|I_{\text{dc}}| \approx 5 \mu\text{A}$. The value of stopping force I_{stop} is given by [4]

$$I_{\text{stop}} = \frac{|I_{\text{c}_-}| - |I_{\text{c}_+}|}{2},$$

In our case, we obtained a value of approximately $-6.1 \mu\text{A}$ for I_{stop} , which closely coincides with our experimental finding of around $-5.5 \mu\text{A}$.

Now we can move on to calculate the output power \bar{P}_{out} by multiplying $\bar{V}_{\text{dc}}(I_{\text{ac}})$ with the corresponding values of I_{dc} as e.g., $\bar{P}_{\text{out}}(I_{\text{ac}}) = \langle V \times I_{\text{dc}} \rangle = \bar{V}_{\text{dc}}(I_{\text{ac}}) \cdot I_{\text{dc}}$. We then measure the input power $\bar{P}_{\text{in}} = \langle V(I(t)) \times I(t) \rangle$ for the applied ac-drive. Finally, we calculate the efficiency using our experimental data. The dependencies of \bar{P}_{in} , \bar{P}_{out} , and η on I_{ac} are shown in Fig. 4.7.

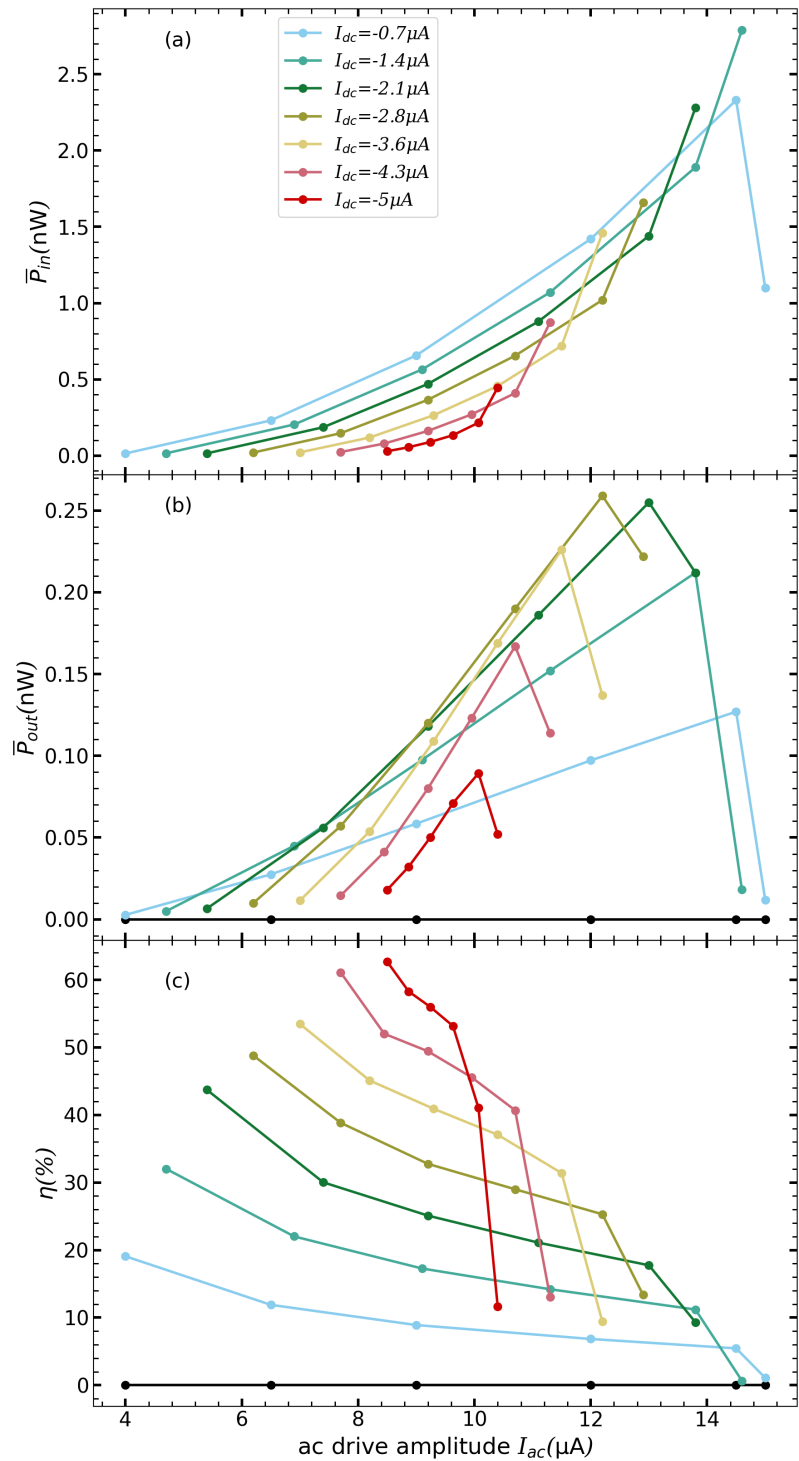


Figure 4.7: (a) $\bar{P}_{in}(I)$. (b) $\bar{P}_{out}(I)$. (c) Efficiency $\eta(I)$.

Measuring \bar{P}_{in} presents a challenging situation as we were unable to extract $I(t)$ from the average or integral, similar to what we did with I_{dc} for \bar{P}_{out} . To overcome this challenge, we manually performed measurements for six I_{ac} values chosen from the curves in Fig. 4.6. For each value, we measured $V(I(t))$ and multiplied it by $I(t)$, followed by integration. The expression for calculating $\bar{P}_{\text{in}}(I_{\text{ac}})$ is given by,

$$\bar{P}_{\text{in}}(I_{\text{ac}}) = \frac{1}{T} \int_0^T V(I(t)) \cdot I(t) dt.$$

The results of these calculations are plotted in Fig. 4.7(a). In Fig. 4.7(b), we observe that increasing I_{dc} leads to an increase in \bar{P}_{out} until $I_{\text{dc}} = -2.8 \mu\text{A}$. Further increases in I_{dc} cause a decrease in \bar{P}_{out} .

Regarding efficiency, as shown in Fig. 4.7(c), we first observe that unlike \bar{P}_{out} , the efficiency constantly increases as the values of I_{dc} increase, while the RW decreases. Furthermore, we note that for every value of I_{dc} , the maximum efficiency occurs at the beginning of the RWs, which is in accordance with the predictions and simulations presented in Chapter 2.

In the next subsection, we will present the simulation results of the ratchet A22 and compare them with its corresponding experimental data.

4.2.1 Numerical Calculations of Ratchet A22's Parameters

In the quasistatic regime, the behaviour of the system is fully defined by the experimental IVC. Therefore, starting from an experimental IVC, one can obtain all the figures of merit. To simulate $\bar{V}_{\text{dc}}(I_{\text{ac}})$, we measure a high-resolution experimental asymmetric IVC, interpolate it, and then we numerically calculate

$$\bar{V}_{\text{dc}}(I_{\text{ac}}) = \frac{1}{T} \int_0^T V(I(t) + I_{\text{dc}}) dt,$$

for the loaded ratchet as shown in Fig. 4.8.

Next, we perform the same with \bar{P}_{in} , \bar{P}_{out} , and finally η , as given by Fig. 4.9. Simultaneously, all numerically obtained plots are compared with their corresponding experimental data.

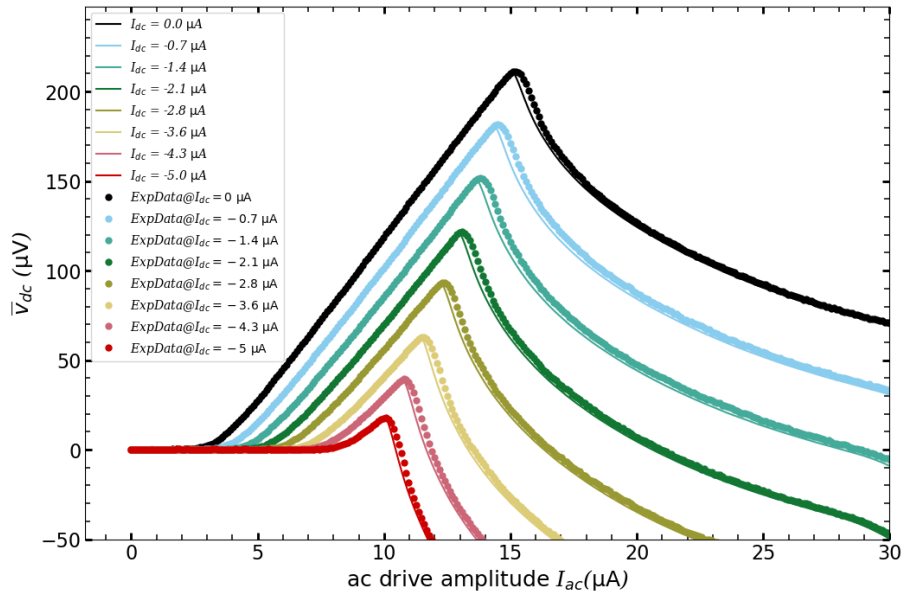


Figure 4.8: Simulations (lines) versus the experimental data (dots) of $\bar{V}_{dc}(I_{ac})$

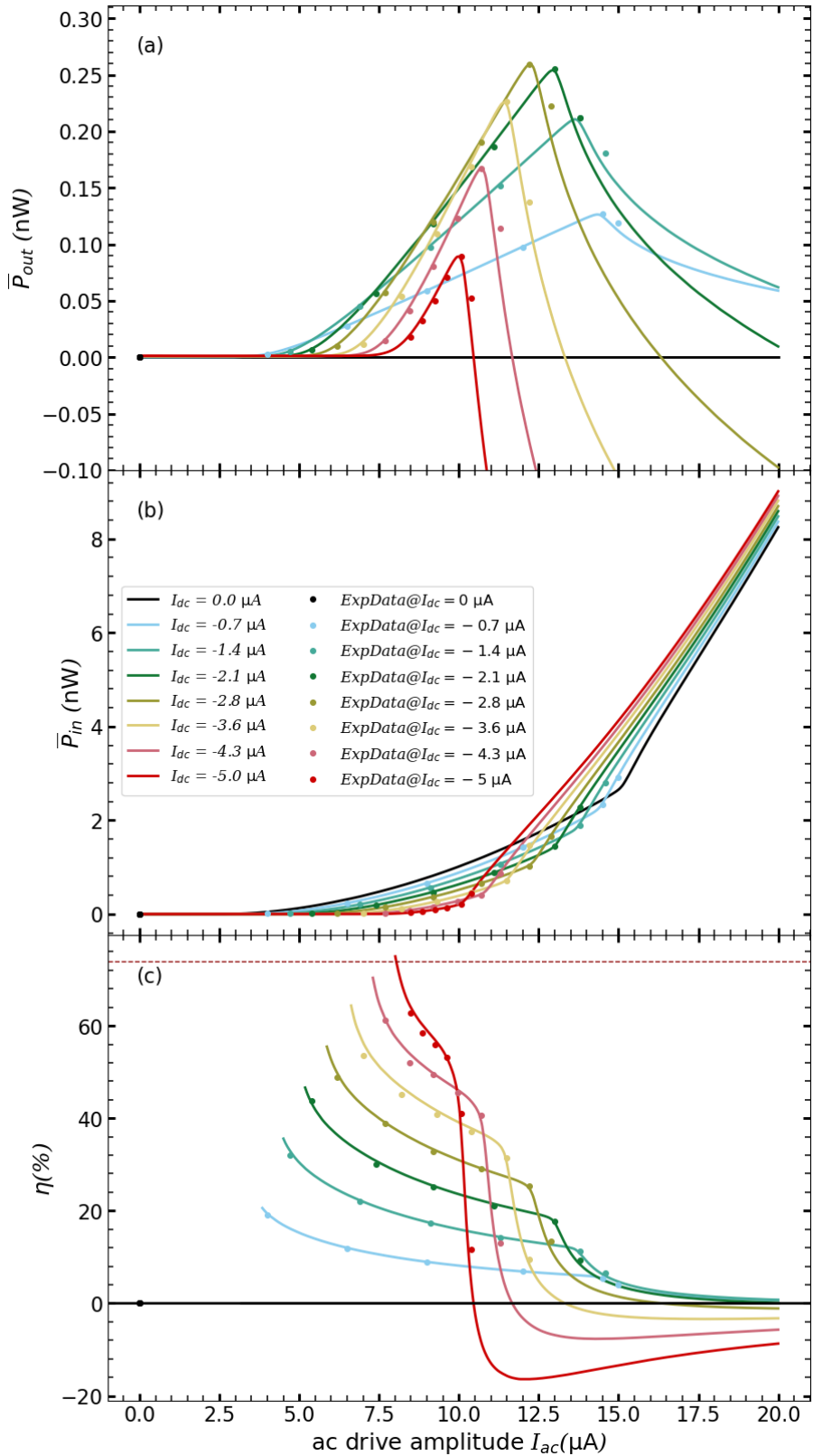


Figure 4.9: Numerical obtained curves (lines) versus the experimental data (dots) of (a) $\bar{P}_{\text{in}}(I_{\text{ac}})$. (b) $\bar{P}_{\text{out}}(I_{\text{ac}})$. (c) $\eta(I_{\text{ac}})$.

One important observation is that, for $I_{\text{ac}} < 2 \dots 3 \mu\text{A}$, the powers approach zero, resulting in the efficiency tending towards infinity with large uncertainty. To address this issue, we impose a cut-off criterion of $P_{\text{in}} \leq 10 \text{ pW}$.

Clearly, we see that our experimental data coincided well with our numerical results based on the experimental IVC. It is enlightening to mention that the theoretical maximum efficiency calculated in [4] (red dashed line in Fig. 4.9(c)) is around 74%, which nicely touches our maximum simulation curve at I_{dc} around stopping current. We also provide a comparison in Table 4.3 to contrast our Josephson ratchet results with existing literature on the Josephson ratchet mechanisms.

4.3 Josephson Ratchet A15

In this section, we will present the experimental results for ratchet A15, similar to the previous section. A comparison between the actual and target parameters is provided in Table 4.2.

A15	Target parameter	Actual parameter
$w(\text{nm})$	300	300
$D(\text{ions/nm})$	507	507
$j_c (\text{kA/cm}^2)$	7.1	53
$I_c(\mu\text{A})$	3.7	28
$\lambda_J(\text{nm})$	250	129
$L(\text{nm})$	1750	1750
$l \equiv L/\lambda_J$	4.9	13.5
f^M	0.25	0.96
$\lambda_J^K(\text{nm})$	2960	1090
$l_K \equiv L/\lambda_J^K$	0.6	1.6
f_K^M	0.09	0.6

Table 4.2: Comparison table of target and actual parameters of ratchet A15.

The IVC of ratchet A15 is shown in Fig. 4.10

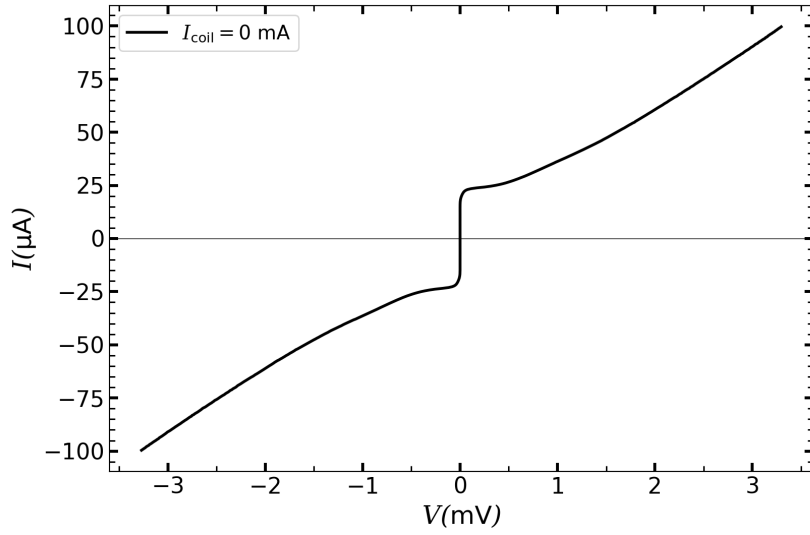


Figure 4.10: IVC of the ratchet A15 at $I_{\text{coil}} = 0$ mA. $|I_{c+}| = |I_{c-}| \approx 21 \mu\text{A}$ and $R_N \approx 32 \Omega$.

As we can see, there is no bending in the IVC as seen in Fig. 4.1, because for A15, we chose $w = 300 \text{ nm}$, and there is no crystal destruction of YBCO due to the distance between the resistive walls. All the other experimental results for this ratchet, similar to the Josephson ratchet A22, are presented in Figs. 4.11 to 4.16.

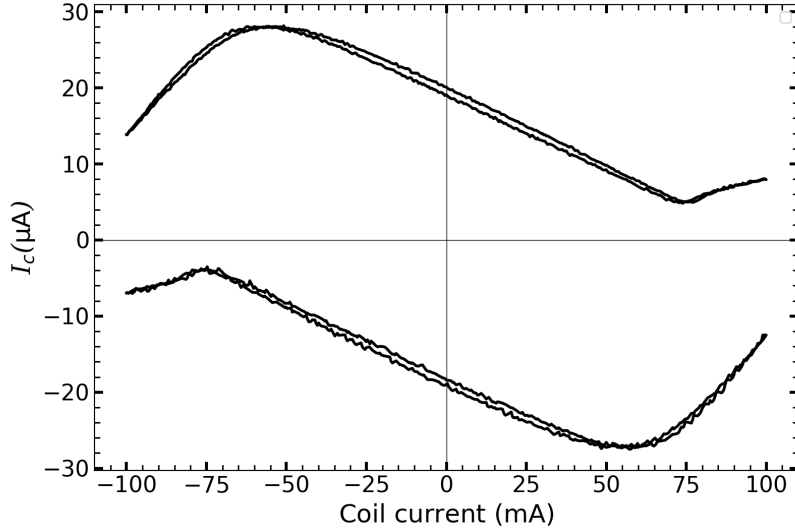


Figure 4.11: Critical current versus magnetic coil current of the ratchet A15.

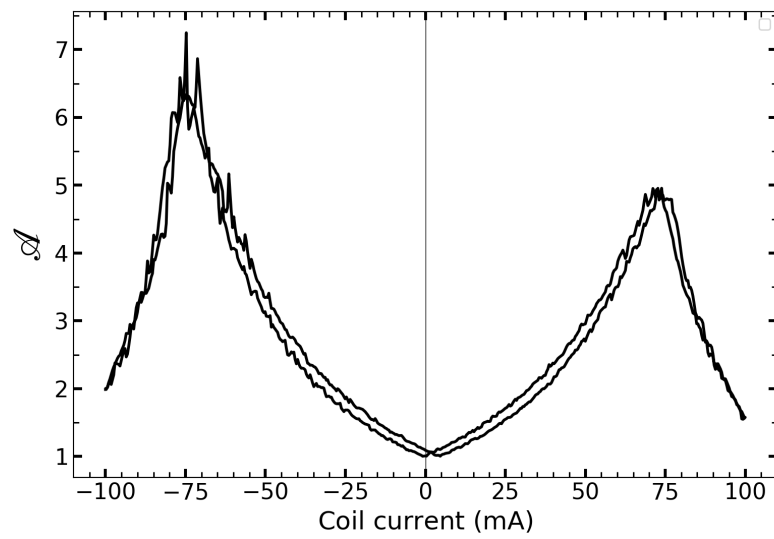


Figure 4.12: The value of asymmetry parameter, which shows the maximum asymmetry $\mathcal{A} \approx 7$ at optimum magnetic $I_{\text{coil}} = 75$ mA.

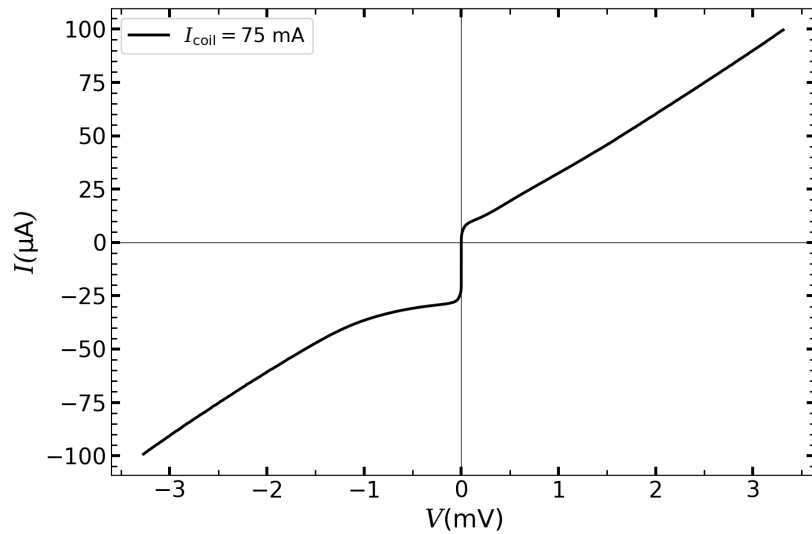


Figure 4.13: An asymmetric IVC of the ratchet A15 at the optimum $I_{\text{coil}} = 75$ mA has $|I_{c_-}| \approx 24.5 \mu\text{A}$ and $|I_{c_+}| \approx 3.5 \mu\text{A}$.

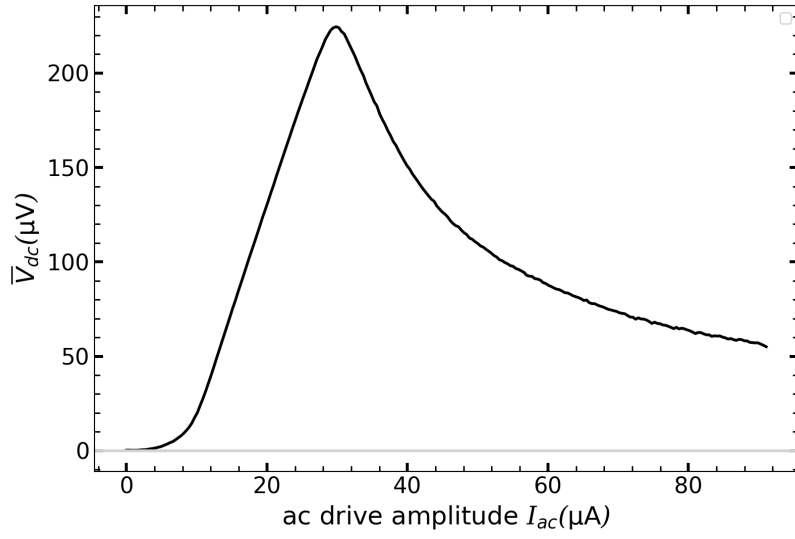


Figure 4.14: The rectification curve $\bar{V}_{dc}(I_{ac})$ for the ratchet A15 at $I_{coil} = 75$ mA with maximum dc average voltage $\bar{V}_{dc}(I_{ac}) \approx 225$ V.

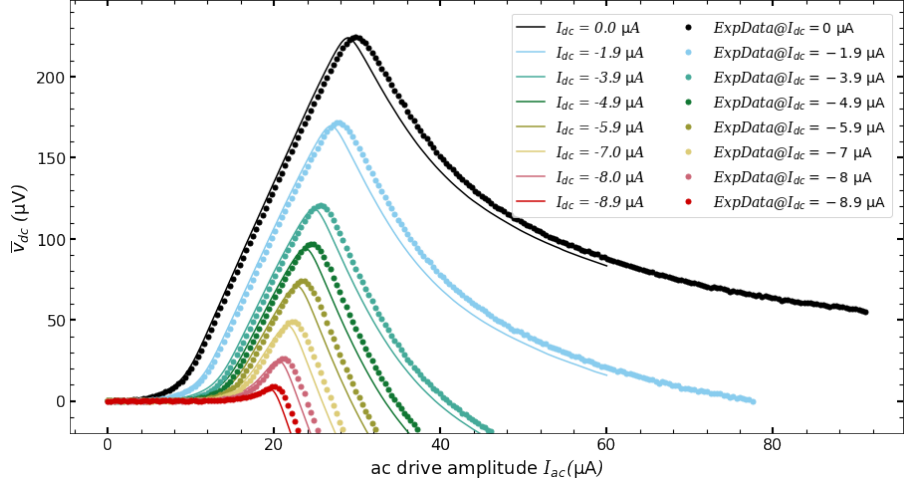


Figure 4.15: Simulations (lines) versus the experimental data (dots) of $\bar{V}_{dc}(I_{ac})$ for the loaded ratchet A15 at $I_{coil} = 75$ mA for several I_{dc} up to stopping force $|I_{dc}| = 8.92$ μ A.

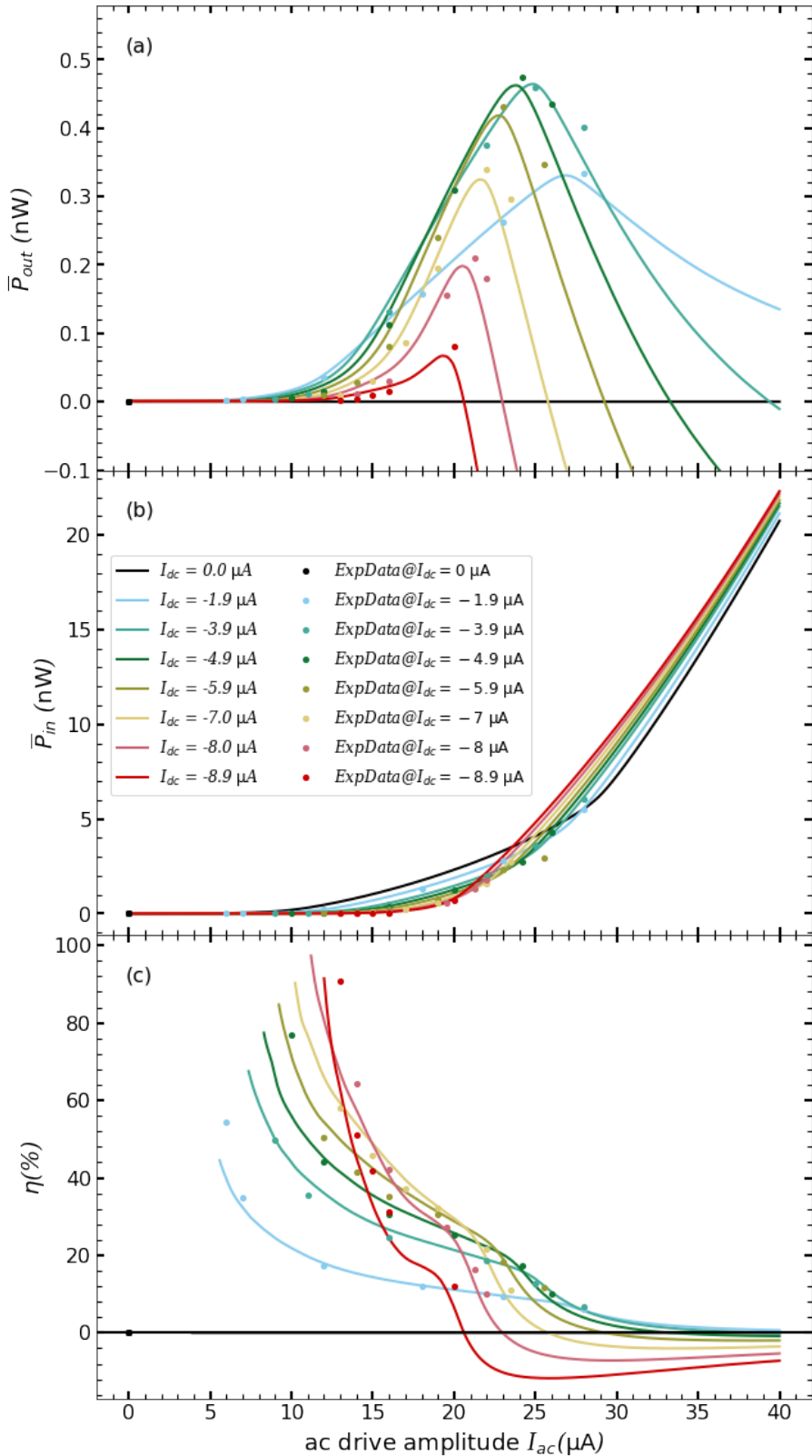


Figure 4.16: Numerical obtained curves (lines) versus the experimental data (dots) of (a) \bar{P}_{in} , (b) \bar{P}_{out} , (c) Efficiency η .

4.4 Driving the Ratchet with a Stochastic Signal

In this section, our objective is to examine the influence of different types of noise on the system and assess their impact. In reality, numerous sources of noise can affect the system and diminish the measurement accuracy. Therefore one of our goal is to use them as a source of energy and rectify them. In this thesis, we explore two distinct types of noise: external and internal noises.

To generate external noise, we consider random normal noises with a Gaussian distribution. For internal noise, we assume it consists of equilibrium thermal fluctuations, which is a thermal noise with a white spectrum, although there may be other sources of noise, such as, $\frac{1}{f}$ noise which is known as brown noise. These sources can include induced signals from radio stations, mobile devices, TV stations, satellites, and so on. Despite working in a screened room, it is not possible to completely eliminate the effect of these noise sources.

4.4.1 External noise

A schematic representation of the stochastic signal and its corresponding distribution can be found in Fig. 4.17,

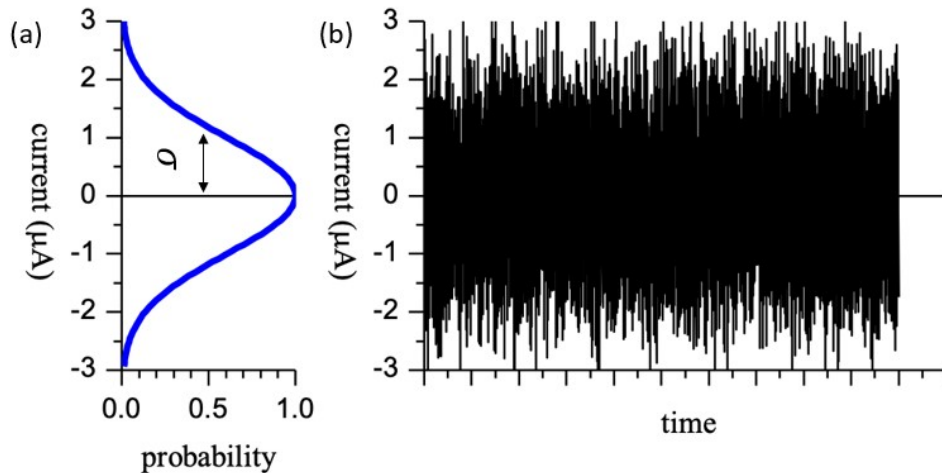


Figure 4.17: (a) The Gaussian distribution of random signal with the width σ . (b) The random signal depends on time.

For the first case, our focus is on examining the impact of external noises through simulation. To accomplish this, we replace the deterministic ac-drive $I(t)$ with an external random signal to drive the ratchet system in a stochastic regime. Since we are operating in the quasistatic regime, we can consider the high-resolution experimental asymmetric IVC of A22 and simulate all the figures of merit by driving the system with the Gaussian signal.

To perform the calculation, we employ a similar procedure to the one used for the ac-drive. However, since we do not have a periodic signal, it is necessary to average

over a long interval. We consider the standard deviation σ as a measure of amplitude of our noisy signal. Due to the ergodicity of the noise, we can substitute the averaging over time by convolution with a Gaussian distribution, as outlined below,²

$$(V * G)(\sigma) = \bar{V}(\sigma, I_{dc}) = \int_{-\infty}^{\infty} V(I + I_{dc}) \cdot G(I, \sigma) dI,$$

where $G(I, \sigma)$ is the Gaussian distribution.³ Similarly we calculate $\bar{P}_{\text{out}}(\sigma, I_{dc}) = \bar{V}_{\text{dc}}(\sigma, I_{dc}) \cdot I_{dc}$ and

$$\bar{P}_{\text{in}}(\sigma, I_{dc}) = \int_{\sigma_{\min}}^{\sigma_{\max}} V(I + I_{dc}) \cdot G(I, \sigma) \cdot I(t) dI.$$

The simulated \bar{V}_{dc} , \bar{P}_{in} , \bar{P}_{out} , and efficiency η of the noisy driven ratchet are presented in Fig. 4.18 and Fig. 4.19 respectively,

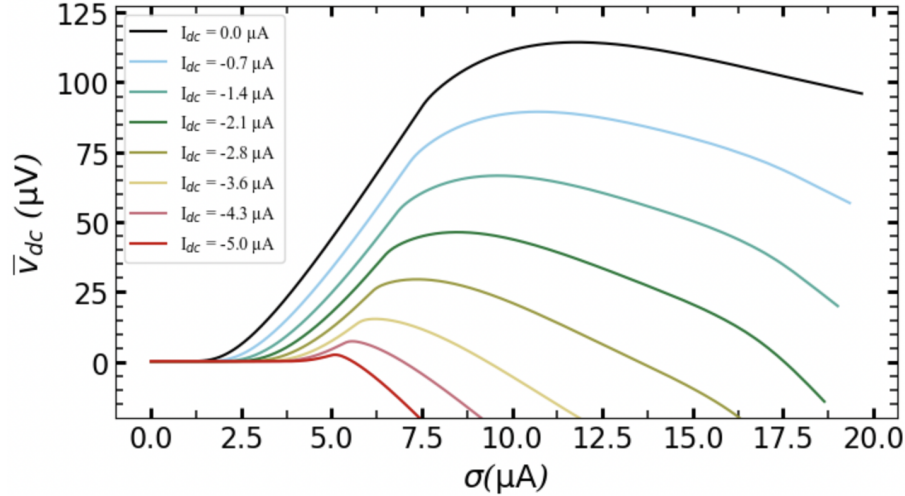


Figure 4.18: Simulation of $\bar{V}_{\text{dc}}(\sigma)$ driven with the Gaussian signal.

²It is important to note that the amplitude of the Gaussian signal is infinite and random. Therefore, we adopt the parameter σ as a measure of the amplitude of our noisy signal.

³Gaussian Distribution can be defined as follow, $G(I, \sigma) = \frac{1}{\sigma\sqrt{2\pi}} \exp\left(\frac{-I^2}{2\sigma^2}\right)$.

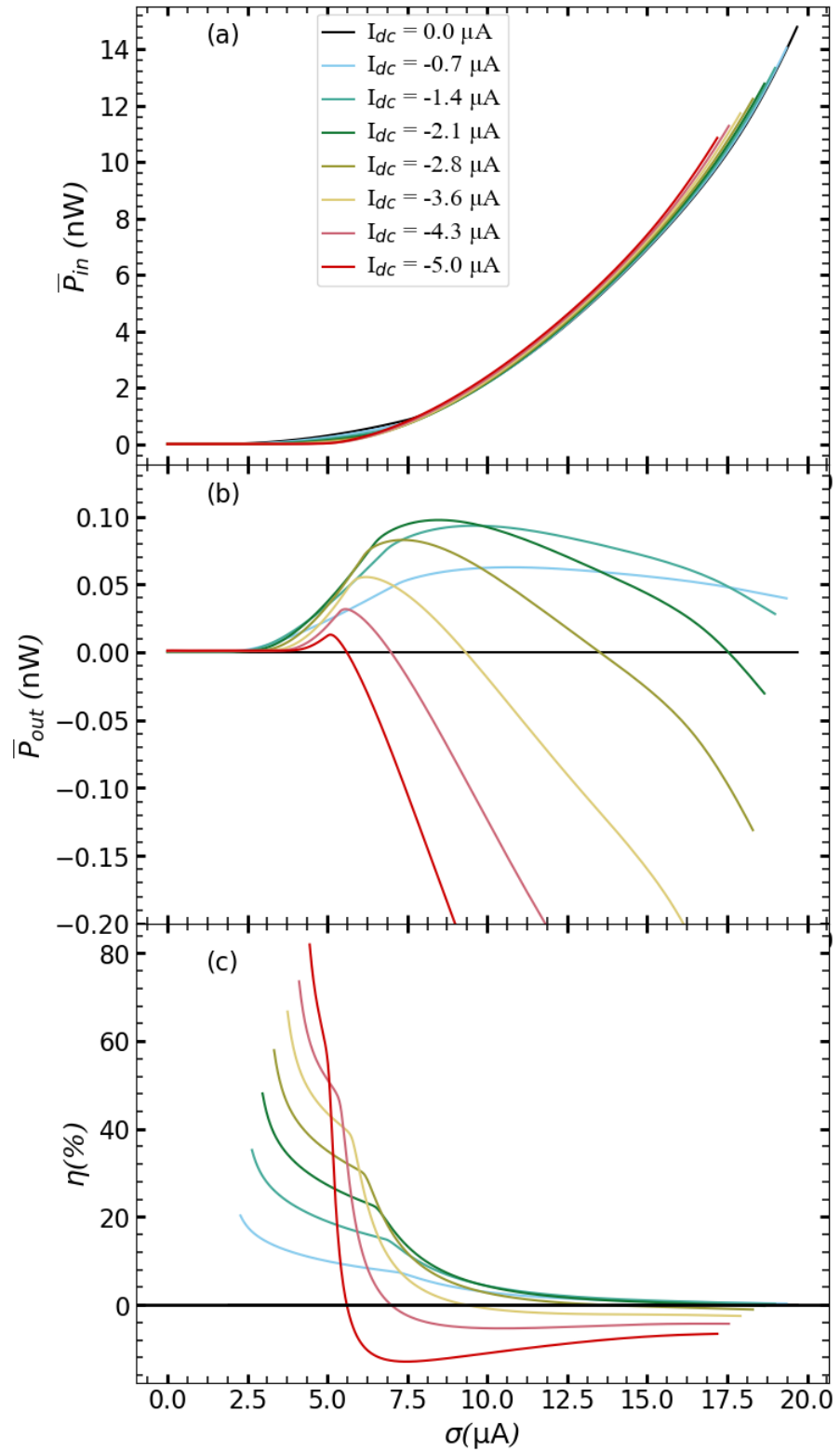


Figure 4.19: (a) $\bar{P}_{in}(\sigma)$. (b) $\bar{P}_{out}(\sigma)$. (c) Efficiency η .

We observe that our Josephson ratchet system remains functional when driven by a random signal instead of a deterministic drive. The figures of merit obtained under the random signal exhibit a similar behavior to those achieved under the deterministic drive. However, the maximum value of the average voltage \bar{V}_{dc} , decreases by a factor of two compared to deterministic drive (ac-drive). Thus, in principle, we drive the system with noise and observe that the noise can also facilitate the transfer of the particle, albeit at a slower pace.

4.4.2 Internal noise

For the case of internal noise, we utilize the inherent noise present within the system, commonly referred to as thermal noise. Thermal noise arises from the random fluctuations due to the thermal energy of the system, specifically in the shunt resistor at a finite temperature. These fluctuations exhibit an amplitude distribution that is nearly Gaussian. The fluctuation-dissipation theorem provides a generic and statistically derived explanation for this phenomenon in the field of statistical physics.

Due to the utilization of high-temperature superconductors (HTSs), our ratchet system can be operated at temperatures up to around 40K. At this temperature, the thermal energy ($k_B T$) is approximately ten times greater compared to when the temperature is 4K. Consequently, the ratchet can be operated with a significantly higher thermal energy level. In the following we present the IVC of the ratchet A15 at temperature around 4.2K and 35K.

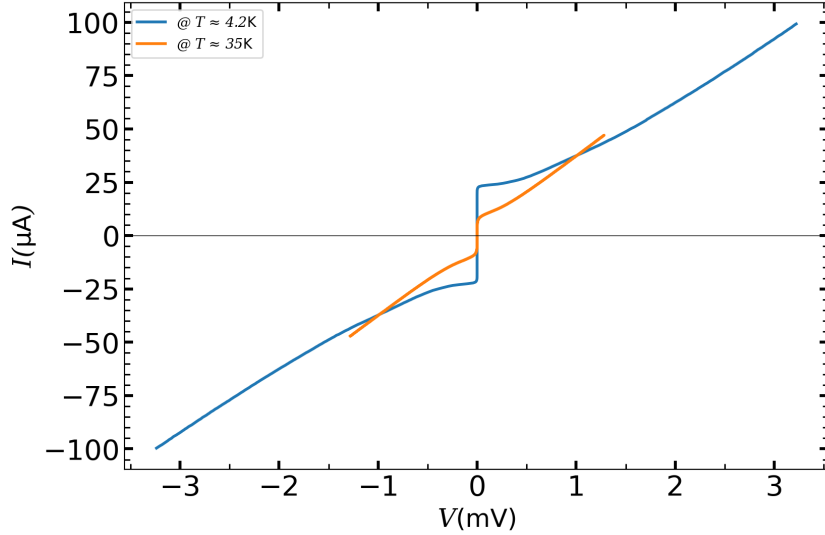


Figure 4.20: IVC of A15 at $T \approx 4.2$ K and 35 K at zero magnetic field $I_{coil} = 0$.

We observe that with increasing temperature, the critical current I_c decreases, while the thermal noise

$$I_{th} = \frac{2\pi k_B T}{\Phi_0} \approx 1.4 \mu\text{A}$$

increases at ($T \approx 30\text{K}$). Consequently, as we approach temperatures in the range of 30-40K, we reach the point where thermal energy becomes comparable to the Josephson energy i.e., the thermal current becomes comparable to the critical current. Now, by applying the optimum magnetic field across the device, we make I_{c+} very small, smaller than the noise current, and therefore strongly smeared on IVC, which can be characterized by the noise parameter (see eq. (1.12)). [9] [13]

Now the very important question is: will asymmetric IVC still cross the origin, or it does not cross the origin due to the rounding around I_{c+} , and one will get $V(0) \neq 0$. The IVC at $B = 0$ and at $B = B_{\text{opt}}$ at $T \approx 35\text{K}$ is shown in Fig. 4.21. Upon zooming in, we confirm that the blue curve does not cross the origin. Thus, the fact that the blue curve does not cross zero indicates that the internal noise is rectified, producing small dc voltage.

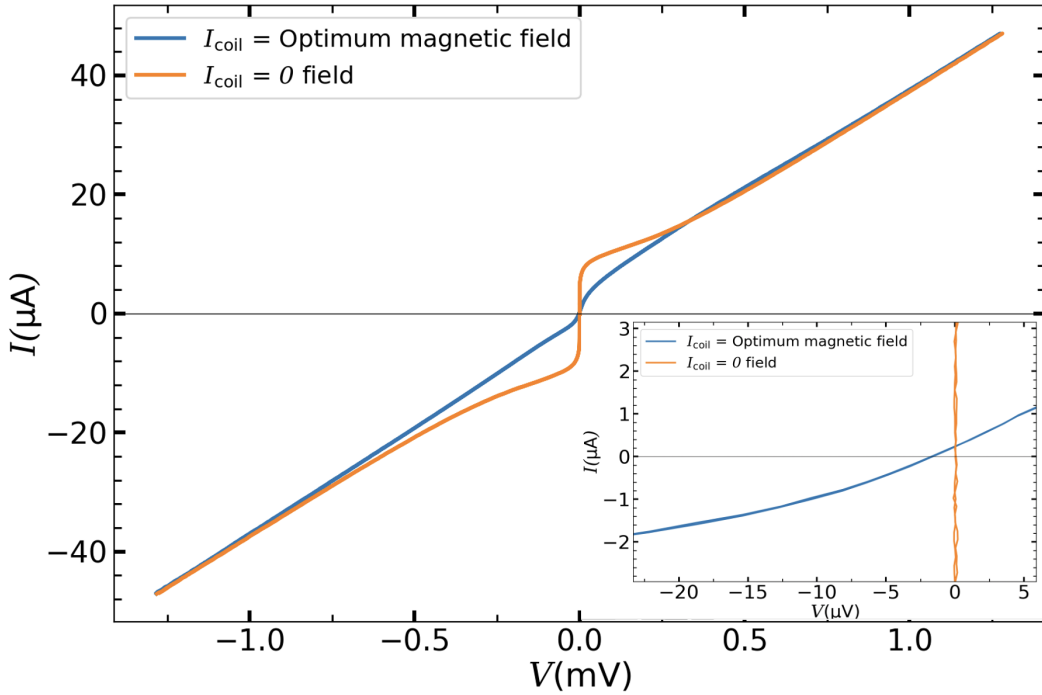


Figure 4.21: IVC for the ratchet A15 at around temperature 35K for the two values of I_{coil} : zero and the optimum magnetic field. In the lower right, we zoom in on the origin.

However, experimentally there can be many pitfalls. In particular, the lack of crossing origin may potentially be attributed to the shift of zero of the current source. To check this possibility, we disconnected the cable from the current source to JJ, and perform an additional measurement, as depicted in Fig. 4.22.

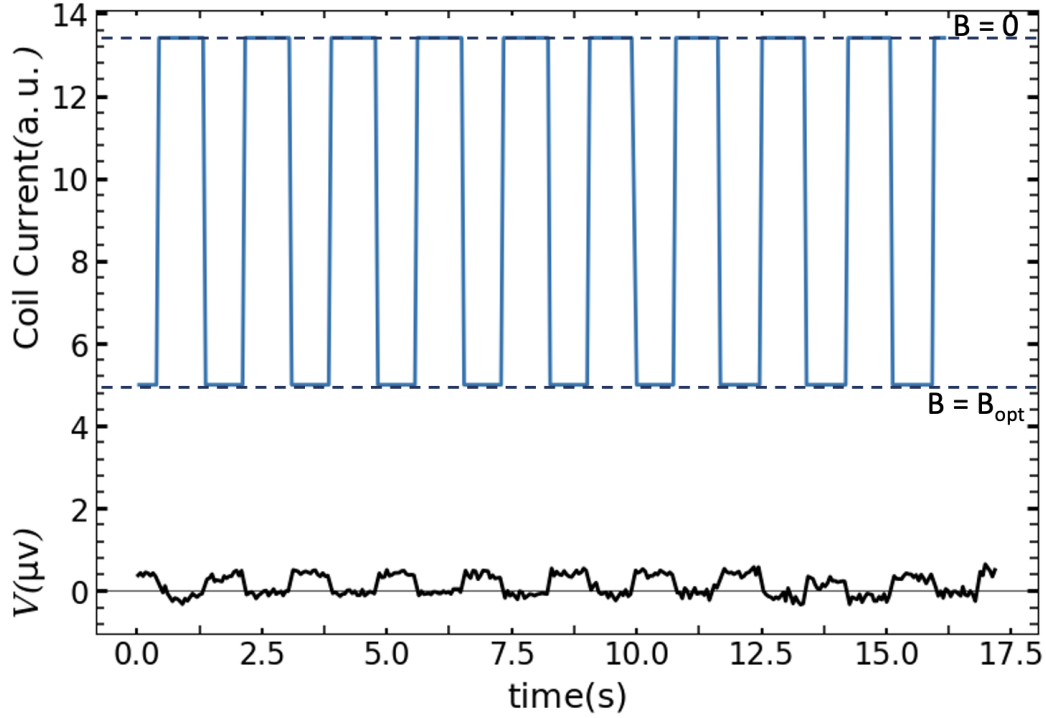


Figure 4.22

In this measurement, we recorded the voltage-versus-time $V(t)$ for device A15 for two cases: when the coil current I_{coil} was set to 0 and when it was set to the optimum value. It was observed that when $I_{\text{coil}} = 0$, there was no voltage response, indicating no rectification effect. However, for the optimum magnetic field, a voltage of approximately $0.4 \mu\text{V}$ was observed. This voltage can be attributed to the rectification effect caused by the noise. A similar effect was reported in a SQUID two decades ago [13].

However, it is known that the rectification of equilibrium thermal fluctuations (e.g., white noise) is prohibited by the second law of thermodynamics. Therefore, the rectification is probably related to some non-equilibrium noise, $\frac{1}{f}$ noise or induce noises from outside. The investigation of the spectral properties of the noise and its role in the rectification process will be a subject of future research and will be explored in forthcoming studies.

4.5 Conclusion and Outlook

Using He-FIB, we successfully fabricated the Josephson ratchet, demonstrated remarkable performance with an efficiency up to 74% based on the asymmetry parameter $\mathcal{A} \approx 7$. The device achieved a maximum average rectified dc voltage $\bar{V}_{dc} \approx 215 \mu V$, with a compact area of around $1 \mu m^2$. To the best of our knowledge, these results represent a record-breaking achievement in the field of Josephson ratchets, as demonstrated by the comparison in Table. 4.3.

Throughout our research, we conducted numerous measurements and simulations to investigate the behavior of the Josephson ratchet under both deterministic and stochastic driving conditions. Finally, we observed the effect of noises in our Josephson ratchet system, which resulted in a small amount of rectified dc voltage being captured in the non-equilibrium regions.

As an **Outlook**, we have several tasks in mind for future research. Firstly, a more detail studies on the effects of noise is required. In particular, investigating the spectrum of the rectified signal and its bandwidth at different noise parameters. Since the influence of noise is subtle, to accomplish this, the fabrication of Josephson ratchets with smaller dimensions and shorter JJ length, while maximizing the asymmetry parameter \mathcal{A} , should be pursued.

Secondly, by achieving a significant number of well-performing ratchets (for example, by improving the quality of BJJJs and minimizing the spread of j_c), one can construct an array of Josephson ratchets to obtain significant rectified dc voltage.

Thirdly, one can develop a new generation of SQUIDs based on in-line geometry of JJ with a periodic asymmetric potential. Surpassing the capabilities of simple Josephson junctions with symmetric potential and investigating the different probable effect of the periodic asymmetric potential into the system at nano scale.

These tasks represent exciting avenues for further exploration and advancement in the field of Josephson ratchets and related technologies.

References	Type	\mathcal{A}	$\bar{V}_{dc}(\mu V)$	$\bar{P}_{out}(nW)$	$\eta(\%)$	Area (μm^2)	$T_{op}(K)$
Carapella (2001) [14]	ALJJ	1.2	5	-	-	44500	6.5
Beck (2005) [15]	ALJJ	2.2	20	-	-	5700	6
Sterck (2005) [16]	3JJ SQUID	2.5	25	-	-	43*	4.2
Sterck (2009) [13]	3JJ SQUID	2.2	25	-	-	1125†	4.2
Wang (2009) [17]	ALJJ	2.8	100	-	-	800	4.2
Knufinke (2012) [1]	ALJJ	4	40	16	25‡	1300	4.2
Menditto (2016) [18]	φ junction	2.5	150	-	-	2000	1.7
Golod (2022) [3]	in-line JJ	4§	8	-	70	7.2¶	7
Paolucci (2023) [19]	2JJ SQUID	3	8	-	6	72	0.4
Thesis (2023)	in-line JJ	7	215	0.2	74	0.9**	4.2

Table 4.3: Comparison key parameters of Josephson ratchet from literature. ALJJ is the abbreviation of annular long JJ, and SQUID is the abbreviation of superconducting quantum interference device.

§ This is the asymmetry at zero magnetic field. The authors claim that the asymmetry at the optimum magnetic field is ~ 10 . In fact, in Fig 3(d) of [3] the asymmetry is around 8.

¶ We approximately calculate the area of the device as $6 \times 1.2 \mu m^2$.

‡ In [1], from Fig. 2 and Fig. 3, we determine that $I_{c-} = -0.5$ and $I_{c+} = 0.3$ in units of $I_0 = 2.8\text{mA}$. We then find $I_{dc}^{\text{opt}} \approx -0.06$ corresponds to maximum \bar{P}_{out} from eq. (18), and substitute this value in eq. (17) to obtain maximum \bar{P}_{out} . Note that, the units in eq. (17) are normalized. Therefore, to convert to physical units, we multiply by $V_1 \cdot I_0 = 280\text{nW}$, where $V_1 \approx 100\mu V$.

* The geometry (Fig. 1 of [16]) is not clearly presented in the paper, so we just summed up the area of the hole and the area of three junctions.

† In Fig. 1(b) of [13], we roughly estimate the size of the device as $45 \times 25 \mu m^2$.

|| From Fig. 2(a) we roughly estimate the area $6 \times 12 \mu m^2$.

** The area we used for this work is $0.45 \times 2 \mu m^2$, see Table. 4.1 and Fig. 3.12.

References

- [1] M. Knufinke, K. Ilin, M. Siegel, D. Koelle, R. Kleiner, and E. Goldobin. "Deterministic Josephson vortex ratchet with a load". *Phys. Rev. E* **85**, 011122 (2012).
- [2] Peter Reimann. "Brownian motors: noisy transport far from equilibrium". *Elsevier*, **361**, Issues 2–4. (2002).
- [3] Taras Golod and Vladimir M. Krasnov. "Demonstration of a superconducting diode-with-memory, operational at zero magnetic field with switchable nonreciprocity". *Nature Communication*, **13**, 3658. (2022).
- [4] E. Goldobin, R. Menditto, D. Koelle, and R. Kleiner. "Model I–V curves and figures of merit of underdamped deterministic josephson ratchets". *Phys. Rev. E* **94**, 032203 (2016).
- [5] Josephson effect. [Wikipedia](#).
- [6] Roderich Tumulka. "Foundations of Quantum Mechanics". *Springer* (2022).
- [7] Ginzburg–Landau theory. [Wikipedia](#).
- [8] Antonio Barone and Gianfranco Paterno. "Physics and applications of Josephson effect", 1982.
- [9] Dieter Kölle. "Basic Properties of Josephson Junctions". *Koelle's Slides*. (2019).
- [10] Jodie Roderiguez. "Characterization of Josephson junctions created by He+ irradiation in commercial Ceraco $\text{YBa}_2\text{Cu}_3\text{O}_{7-x}$ thin films", 2022. Bachelor thesis.
- [11] B. Müller, M. Karrer, F. Limberger, M. Becker, B. Schröppel, C.J. Burkhardt, R. Kleiner, E. Goldobin, and D. Koelle. "Josephson Junctions and SQUIDs Created by Focused Helium-Ion-Beam Irradiation of $\text{YBa}_2\text{Cu}_3\text{O}_7$ ". *Phys. Rev. Applied* **11**, 044082 (2019).
- [12] V. V. Dobrovitski V. G. Kogan, J. R. Clem, Yasunori Mawatari, and R. G. Mints. "Josephson junction in a thin film. *Phys. Rev. B* **63**, 144501 (2001).
- [13] Kleiner R. Sterck A, Koelle D. "Rectification in a stochastically driven three-junction SQUIDs rocking ratchet". *Phys. Rev. Lett.* **103**, 047001 (2009).

- [14] G. Carapella and G Costabile. "Ratchet effect: Demonstration of a Relativistic Fluxon diode". *Phys. Rev. Lett.* **87**, 077002 (2001).
- [15] M. Beck, E. Goldobin, M. Neuhaus, M. Siegel, R. Kleiner, and D. Koelle. "High-Efficiency Deterministic Josephson Vortex Ratchet". *Phys. Rev. Lett.* **95**, 090603 (2005).
- [16] A. Sterck, R. Kleiner, and D. Koelle. "Three-junction SQUID Rocking Ratchet". *Phys. Rev. Lett.* **95**, 177006 (2005).
- [17] H. B. Wang, B. Y. Zhu, C. Gürlich, M. Ruoff, S. Kim, T. Hatano, B. R. Zhao, Z. X. Zhao, E. Goldobin, D. Koelle, and R. Kleiner. "Fast Josephson vortex ratchet made of intrinsic Josephson junctions in $\text{Bi}_2\text{Sr}_2\text{CaCu}_2\text{O}_8$ ". *Phys. Rev. B* **80**, 224507 (2009).
- [18] R. Menditto, H. Sickinger, M. Weides, H. Kohlstedt, D. Koelle, R. Kleiner, and E. Goldobin. "Tunable φ Josephson junction ratchet". *Phys. Rev. E* **94**, 042202 (2016).
- [19] F. Giazotto F. Paolucci, G. De Simoni. "A gate- and flux-controlled supercurrent diode effect". *Appl. Phys. Lett.* **122**, 042601 (2023).